

The Cellular Potts Model on Disordered Lattices

Hossein Nemati* and Joost de Graaf

*Institute for Theoretical Physics, Center for Extreme Matter and Emergent Phenomena,
Utrecht University, Princetonplein 5, 3584 CC Utrecht, The Netherlands.*

(Dated: April 16, 2024)

The Cellular Potts model, also known as Glazier-Graner-Hogeweg model, is a lattice-based approach, by which biological tissues at the level of individual cells can be numerically studied. Traditionally, a square or hexagonal underlying lattice structure is assumed for two-dimensional systems and this is known to introduce artifacts in the structure and dynamics of the model tissues. Here, we developed a new variant of this method that can be applied to a broad class of (ir)regular lattices. We show that on an irregular lattice, deriving from a fluid-like configuration, two types of artifacts can be removed. We further report on the transition between a fluid-like disordered and a solid-like hexagonally ordered phase present for monodisperse confluent cells as a function of their surface tension. This transition shows the hallmarks of a first-order phase transition, and is different from the glass/jamming transitions commonly reported for the vertex and Voronoi models. We emphasize this by analyzing the distribution of shape parameters found in our state space. Our analysis provides a useful reference for the future study of epithelia using the (ir)regular Cellular Potts model.

I. Introduction

Collective cell migration plays an essential role in many biological settings, ranging from morphogenesis [1–5], to wound healing [6–9], to cancer metastasis [4, 10–15]. Confluent cell monolayers, such as those found in epithelial tissues, have attracted considerable attention from the modeling community. Firstly, their effective two-dimensional (2D) nature makes them relatively simple to study, yet these tissues can exhibit a wide variety of collective [9, 10, 16, 17] and rheological [18–23] behaviors. Secondly, the fact that epithelia form the outer surfaces of our organs, makes them susceptible to cancer [24, 25] and play a role in a wide variety of diseases [26–28], including pulmonary fibrosis [29] and asthma [19]. This gives the study of epithelia a direct biomedical relevance.

Over the past decades, various quantitative (computational) models have been developed that capture the principal features of cell populations, without being overburdened by complexity [30, 31]. Many are agent-based in nature and have seen concurrent use in the study of active matter [32]. For tissues and cells, these models include lattice-based methods like cellular Potts model (CPM) [33–40] and cellular automata (CA) [41–44], particle-based [3, 45–48], vertex [18, 49–52], Voronoi [53–56], phase-field [57–63], and Fourier-contour models [64]. Evolutionary dynamics can also be included in models to account for (cancerous) mutations and invasion [65–69]. We refer to Refs. 11, 30, 57, 70 for overviews of the different models available and their respective ranges of application. Ref. 11 provides a detailed list of open-source implementations of these models, should one wish to experiment. Lastly, Refs. 71, 72 have made comparisons between different models, which included their ability to describe cell shapes and the way cells exchange neighbors.

In this paper, we will limit ourselves to the CPM, which has good performance on these two points. For example, the CPM has been successfully used to study cell sorting and rearrangements [33, 73, 74], chemotaxis [75–77], topotaxis [78], cell migration patterns [79–83], wound closure [84, 85], tumor growth and invasion [37], and the interactions of cells with extracellular matrix [86–88]. Several open-source packages are available for using the CPM [89–94] and the approach has been extensively reviewed, *e.g.*, see Refs. 34–36, 95. However, despite its popularity and qualities, the method is known to suffer from lattice artifacts [36] and can have a relatively high computational cost [71, 72]. Some of the known issues have been addressed. For example, cells can be fragmented at a sufficiently high rate of cell membrane fluctuations (low surface tension). This was resolved by Durand and Guesnet [96] by adding an efficient connectivity check. In addition, a node-based version of CPM has been recently proposed with the goal of reducing lattice artifacts [97]. This model describes the cells as polygons and tracks their vertices.

We will take a different route toward removing/reducing lattice artifacts. We employ an irregular and on-average homogeneous lattice to support our CPM, which derives from a separate simulation of a fluid-like state *via* Voronoi tessellation. Using this supporting lattice, we study how the absence of long-range order in the lattice affects the transition between (disordered) fluid-like and solid-like states that can occur in model epithelia. Such changes of state are experimentally reported to include *jamming*, *rigidity*, and *glass transitions* [14, 19, 98–104], and reproduced in a variety of vertex- and Voronoi-based computational studies [18, 53, 105–107]. These transitions have attracted attention as key players in the development of the aforementioned tissue-related diseases. The change from fluid-like to solid-like is commonly referred to as a *phase transition* in the literature [14, 19, 103, 108, 109] and we adopt the nomenclature. Note, however, that biolog-

* h.nemati@uu.nl

ical tissues are intrinsically out of equilibrium.

Disordered arrested dynamics and fluid-to-solid transitions have been reported for the CPM [110–112]. However, Durand and Heu [113] used the CPM to study soft cellular systems and instead found an order-to-disorder phase transition. We revisit the work by Chiang and Marenduzzo [110], and show that lattice artifacts present in their systems are removed by our irregular-lattice CPM. Our results further demonstrate that there is an order-to-disorder transition for the base CPM, rather than one based on a disordered dynamic arrest. This transition has all the hallmarks of a first-order phase transition from a fluid to a hexagonal solid. We verified the nature of the transition by examining in detail the geometric features of the cells in the tissue and their neighborhoods. Such features include the (distribution of) the isoperimetric quotient and the circularity. We have also studied how our irregular lattice compares to the use of a hexagonal one and find that the latter has spurious dynamics in the hexagonal crystal state.

The benefits of using a CPM on an irregular lattice come at only a small computational overhead compared to using the regular CPM. This makes it a suitable alternative for the study of real biological tissues, which we aim to pursue in future work.

II. Methodology

In this section, we cover the main features of our variant of CPM: the creation and characterization of irregular lattices, and the means by which we have modified the traditional CPM to work with these lattices. We also discuss the various means, including the mean-squared displacement (MSD) and isoperimetric quotient, by which we characterize the outcomes of our simulations. We further provide our standard choices for the system parameters and simulation ranges that we have considered.

A. The Cellular Potts Model

We introduce the basic CPM algorithm here so that the background for our extension is set. Assume that we have a lattice with N_s sites and N_c cells, we can define a function $\sigma : \{1, \dots, N_s\} \mapsto \{1, \dots, N_c\}$ that describes the configuration of the cells on the lattice, uniquely. That is, $\sigma(i)$ indicates the cell index, to which the site i of the lattice belongs. As the development of CPM was inspired by the Potts model [114] — originally used to study spin systems — let us call $\sigma(i)$ the *spin* of site i . Note that the real biological system of interest for the CPM has nothing to do with magnetism and the spin indices.

Now that we can describe a configuration using σ , we can specify the Hamiltonian that gives the total energy of the system, $H = H(\sigma, \mathcal{P})$, where \mathcal{P} represents the set of all physical parameters of the system, e.g., surface tension and target cell area. In general, the lattice can be of any dimension, but we will restrict ourselves to 2D CPMs here. These are suited to describe cell monolayers, which form a class of epithelia, found in the cells lining blood vessels and alveolar sacs of the lung [115]. The simplest

form of Hamiltonian that is used on 2D regular lattices is given by

$$H = \frac{\alpha}{2} \sum_{i=1}^{N_s} \sum_{j \in \mathcal{N}(i)} (1 - \delta_{\sigma(i), \sigma(j)}) + \lambda \sum_{\sigma=1}^{N_c} (a_\sigma - A_0)^2. \quad (1)$$

This equation has two terms on its right-hand side.

The first gives the total interaction energy between the cells that comes from the surface tension between the cell membranes. The indices i and j indicate the lattice sites and the summation is carried out over the site pairs within each other's *interaction neighborhood*. The Kronecker delta δ_{ij} (1 if $i = j$ and 0 if $i \neq j$ for any indices) is used to indicate that only adjacent sites that belong to cells with different spins contribute to the surface tension. The factor α indicates the surface tension and is typically considered uniform between cells, though the method can be used to study mixtures of different cell types as well [33, 73, 116].

The second term indicates that each cell has a preferred (or target) area A_0 . Departures of the instantaneous area a_σ away from A_0 are penalized using a Hookean potential with spring constant 2λ . This choice models the tendency of cells to have a constant volume, as well as their connection to their neighbors within an epithelium. That is, any change in shape (elongation / shrinking out of the plane) will lead to a change in the in-plane area (volume conservation). It is assumed that any deviation from the natural shape is associated with an energy cost, which at the lowest order would be quadratic.

The ‘dynamics’ of the CPM is propagated using a Monte-Carlo (MC) approach. This consists of trial moves weighted by the change in the energy. A trial move involves changing the spin of a randomly chosen site to that of its neighbors. In brief, the basic implementation is

1. Store the energy of the current configuration $E_{\text{old}} = H(\sigma_{\text{old}}, \mathcal{P})$ and choose a lattice site randomly, say, site i . We call it the *candidate site*.
2. Choose a site from its surroundings¹, $\mathcal{N}_c(i)$, say, site j . We call it the *invading site*.
3. If $\sigma(i) = \sigma(j)$, go to step 1. Otherwise, temporarily change $\sigma(i)$ into $\sigma(j)$, and calculate the new value of energy, $E_{\text{new}} = H(\sigma_{\text{new}}, \mathcal{P})$. We call this configurational change an *attempt*.
4. Call the change in energy $\Delta E = E_{\text{new}} - E_{\text{old}}$. When $\Delta E \leq 0$, accept the attempt. When $\Delta E > 0$, accept

¹ This neighborhood $\mathcal{N}_c(i)$ is not necessarily the same as the one used for the computation of the Hamiltonian $\mathcal{N}(i)$ and may be defined separately.

the attempt with the probability

$$P_{\text{acc}} = \exp\left(-\frac{\Delta E}{k_B T}\right), \quad (2)$$

or reject it with probability $1 - P_{\text{acc}}$. Here, the energy difference is normalized by the thermal energy, where k_B is the Boltzmann constant and T is the temperature. Go to step 1.

It should be noted that the use of thermal energy in the algorithm, reflects its origin as a tool to study spin systems. The interpretation of the temperature in the context of a cell membrane is to set a rate, at which the various (internal) cell activities change the boundaries. This rate can be given the interpretation of a time scale for membrane fluctuations [36, 74, 96], provided only local trial moves are used. Nonetheless, the CPM's dynamics do not represent the evolution of the system, as would follow from say a Langevin description.

According to the algorithm above, the site pairs which belong to the same cell, are also allowed to be chosen. Such picks are always disregarded for updates after checking that the spins are the same. However, picking these pairs comes at a computational cost. It is possible to identify all 'allowed site pairs' in *linked list* data structures [117] and only choose from the elements of these lists. However, in practice, for our typical parameter choices, it turned out that searching and updating the linked lists was computationally disadvantageous. Hence, we utilized the above algorithm. Note that linked lists should become more efficient when the number of border sites is considerably less than the total number of lattice sites. Examples of this include the simulation of single cells [118] and non-confluent cell populations [119, 120].

B. Using (Ir)regular Lattices

The above algorithm for site updates holds for *any* underlying lattice, provided $H(\sigma, \mathcal{P})$ and $\mathcal{N}_c(i)$ for $1 \leq i \leq N_s$ are well-defined. However, as mentioned in the introduction, to our best knowledge, CPM has only been applied to regular lattices, *i.e.*, square and hexagonal lattices². When moving to irregular lattices, we will assume that for any lattice site i , we have $\mathcal{N}_c(i) = \mathcal{N}(i)$. In addition, we have assumed that the sites i and j are neighbors to each other, if and only if the polygons that contain these sites have at least one vertex in common. This simple rule on square lattice leads to Moore neighborhood which considers 8 neighbors for each site, see Fig. 1a. On a hexagonal lattice, this leads to six neighbors, while the number of neighbors will vary per site on an irregular lattice, see Fig. 1b,c, respectively. All of the neighborhoods considered thus far are in contact with the central

cell. This is intuitive, as the interaction term considered in the CPM Hamiltonian describes surface tension. For discussion on other definitions of a neighborhood (for regular lattices) we refer to, for example, Refs. 96, 121.

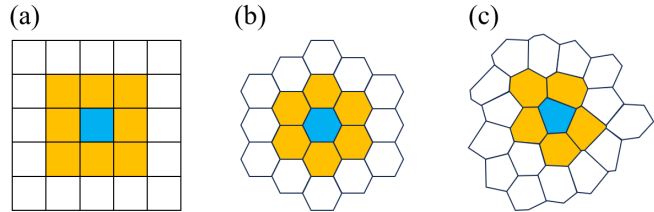


Figure 1. The definition of a neighborhood on different lattice types. (a) The Moore neighborhood on a square lattice, where the central site is blue and its 8 neighbors are indicated in yellow. (b) On the hexagonal lattice, there are 6 nearest neighbors to a central site. (c) On the irregular lattice, the sites having at least one shared vertex are neighbors.

To work with an irregular lattice, the Hamiltonian of Eq. (1) needs to be modified. As the surface energy is proportional to the contact length of cells, we introduce a weight factor in the interaction term of the Hamiltonian. This weight ensures that the surface-energy penalty is proportional to the contact length of neighboring sites. The Hamiltonian then reads

$$H = \alpha \sum_{\langle i,j \rangle} w_{ij} (1 - \delta_{\sigma(i), \sigma(j)}) + \lambda \sum_{\sigma=1}^{N_c} (a_{\sigma} - A_0)^2, \quad (3)$$

in which the notation is mostly the same as in Eq. (1). Here, the first summation on the right-hand side runs over all neighboring sites based on the aforementioned neighborhood, and w_{ij} is the weight factor shared between sites i and j . This weight is defined

$$w_{ij} = l_{ij}/\bar{l}, \quad (4)$$

where l_{ij} is the length of the contact edge between the sites i and j , and \bar{l} is the average length of the edges taken over the entire lattice. Taking $w_{ij} = 1$, which is appropriate for regular lattices, the Hamiltonian of Eq. (3) reduces to that of Eq. (1).

We generate our irregular lattices from a set of points using Voronoi tessellation. There are many ways in which to choose the generating points, *e.g.*, by choosing these randomly on the plane using a uniform distribution. However, this leads to the presence of many small Voronoi cells and several large ones [122, 123]. Here, we want our lattice sites to have roughly the same size and number of neighbors, whilst maintaining an isotropic character to the distribution of points. Therefore, we choose to base our lattice on the center of mass (CMS) of uniformly sized particles in a fluid phase. A regular CPM can be easily implemented and can serve to generate such a configuration for a suitably chosen value of $\alpha = 0.8$, which places the configuration in the fluid phase. We performed a large-scale simulation to obtain

² Except the node-based version of CPM [97] which describes cells through surfaces rather than through volumes, making it principally different to the standard CPM.

an equilibrated fluid, see Table I for our choices, by which we obtained approximately 200^2 lattice centers. This is illustrated in figure 2a³.

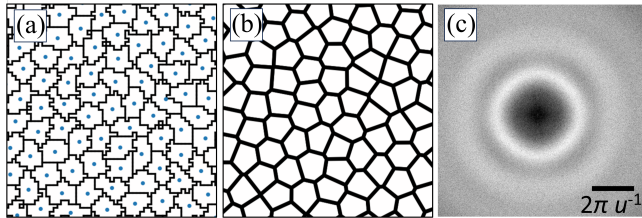


Figure 2. Creation and characterization of the irregular lattice. (a) Part of a snapshot of the simulation, which was used to create a fluid state of cells. Nearly 0.1% of all simulated cells are shown, outlined in black. The blue dots indicate the cell’s centers of mass. (b) The Voronoi tessellation based on the snapshot in panel a. Each polygon will serve as a lattice site for our irregular lattice. (c) Fast Fourier transform of the picture of the center of mass of all cells comprising the fluid-like state — a portion of which is shown in panel a. We express the inverse wave length in terms of a length unit u , which represents the average cell spacing.

Next, we applied Voronoi tessellation to these centers, imposing periodic boundary conditions, using the package `Voro++` [124], see figure 2b. Finally, we verified that the newly formed irregular lattice does not have any long-range orientational structure. Using the image analysis software `ImageJ` [125], we performed a fast Fourier transform (FFT) on a snapshot of the center of mass of the lattice sites. The result is shown in figure 2c, which reveals the uniform rings, that are indicative of structural homogeneity. Further simulation details will be provided in Section II C.

C. Simulation Parameters

The dynamics of the system is generated through MC attempts, as described in Section II A. We refer to N_s MC attempts as a *sweep* and we measure ‘time’ in terms of MC sweeps (MCS). As the temperature here is merely a scaling of the cell membrane fluctuations, we set $k_B T = 1$ throughout. The number of MCSs used depends strongly on the state point under consideration since the system features slow dynamics. Table I provides the relevant choices for both the equilibration (or waiting) time t_w and the time over which we sampled t_s . We examined the evolution of total energy, the shape parameters, and the order parameter, both of which will be introduced shortly, to establish the appropriate value of t_w .

We wanted to evaluate the phase transition induced by the variation in the surface tension of the cells. Therefore, we assumed λ to be constant and equal to 1.0, while

³ For this study, we did not need to introduce any specific length unit. Lengths may be subsumed in the definitions of the prefactors. Only for the fast Fourier transforms, we introduce the length scale u , which makes the wave space vectors scale as u^{-1} .

we changed α as the control parameter in the range of $\alpha \in [1.0, 4.0]$ on all lattices, to go from a disordered diffusive dynamics of the cells to an ordered arrested one. The value of α was changed in steps of 0.2, and smaller steps of $(0.02 \sim 0.04)$ near the transition point, as appropriate. In all cases, we used periodic boundary conditions and modeled nearly 1000 cells, see Table I for the details. For the irregular lattice, we used a simulation box of size $L_x = 200.11$ and $L_y = 197.08$, such that it is perfectly tileable by hexagons having a target area of $A_0 = 40$. Every configuration studied was set up (and remained) confluent. We also performed several independent simulations to generate statistics.

D. Characterization of the Results

We characterize the outcomes of our simulations in several ways. First, we compute the MSD, $\langle r^2(t) \rangle$, by extracting the CMS of each cell after equilibrating the system. Here, r measures the displacement, the brackets indicate an ensemble average, and we have introduced the time t . Henceforth, we identify t as the number of MCS⁴. The MSD was then computed from the CMS displacements in the usual fashion[53]. We also fitted power-laws to the extracted MSDs to evaluate the diffusive behavior of the cells. Here, we focused on the long-time behavior only, which we found to follow

$$\langle r^2(t) \rangle \propto t^\beta, \quad (5)$$

where β is the scaling coefficient. In practice, we determined β from the slope of the MSD after taking the log of both the time and MSD. To calculate the effective diffusion coefficient D_{eff} , we use

$$\langle r^2(t) \rangle = 4D_{\text{eff}}t, \quad (6)$$

for the long-time behavior, whenever $\beta \gtrsim 0.95$.

Second, we consider the local bond-order parameters to establish the degree of hexatic order. This is computed as follows for the cell indexed k

$$\psi_6(k) = \frac{1}{N_n} \sum_{j \in \mathcal{N}(k)} e^{6i\theta(j,k)}. \quad (7)$$

In this equation, $\mathcal{N}(k)$ is the set of nearest neighbors to the k -th cell and N_n is the number of neighbors. Here, $\mathcal{N}(k)$ is considered simply six nearest neighbors⁵ of the cell k . This means that $N_n = 6$ for all the cells. The angles $\theta(j,k)$ represent the counterclockwise angle between the x -axis and the vector connecting the center-of-mass of the cell k to that of j . The i represents the complex iden-

⁴ This definition is subject to the caveat that MCS can be understood to be proportional to the real time in a system, but they are not the actual time.

⁵ Other definitions of the local hexatic bond order are possible [126, 127], but we considered the definition provided in Eq. (7) the most appropriate for our purposes.

Table I. Parameter choices and details of the simulations carried out for this study. These include the size of the simulation boxes ($L_x \times L_y$), the number of lattice sites (N_s) and number of cells (N_c), the preferred cell area (A_0) and the values of surface tension (α). Waiting and sampling times (t_w and t_s), and the number of independent simulations for each value of α are presented in the final three rows, specified by α . The right-most column presents the values for the square-lattice simulation, by which we generated the fluid state from which the irregular lattice was obtained.

	square	hexagonal	irregular	irr. gen.
$L_x \times L_y$	200^2	199.15×199.87	200.11×197.08	1280^2
N_s	4×10^4	39804	40960	1280^2
N_c	1000	1000	986	40960
A_0	40	39.80	40	40
α	[1, 4]	[1, 4]	[1, 4]	0.8
t_w (MCS)	$3 \times 10^5 \sim 6 \times 10^5, \alpha \in [1, 1.8]$ $1 \times 10^6 \sim 3 \times 10^6, \alpha \in [2, 2.8]$ $8 \times 10^6, \alpha \in [3, 4]$	$3 \times 10^5, \alpha \in [1, 2.2]$ $1 \times 10^6, \alpha \in [2.4, 4]$	$3 \times 10^5 \sim 7 \times 10^5, \alpha \in [1, 2.28]$ $1 \times 10^6, \alpha \in [2.4, 4]$	2×10^4
t_s (MCS)	$2 \times 10^5 \sim 4 \times 10^5, \alpha \in [1, 1.8]$ $1 \times 10^6, \alpha \in [2, 2.4]$ $2 \times 10^6, \alpha \in [2.6, 4]$	$2 \times 10^5, \alpha \in [1, 1.8]$ $7 \times 10^5, \alpha \in [2, 2.2]$ $1 \times 10^6, \alpha \in [2.4, 4]$	$2 \times 10^5 \sim 3 \times 10^5, \alpha \in [1, 2.28]$ $1 \times 10^6, \alpha \in [2.4, 4]$	–
Number of simulations per each α	50	20	20	1

tity, $\iota^2 = -1$. For a perfect hexagonal arrangement, the absolute $|\psi_6(k)| = 1$, and the value of the hexatic order decreases with disorder. Typically, we average $|\psi_6|$ over all cells and the production time.

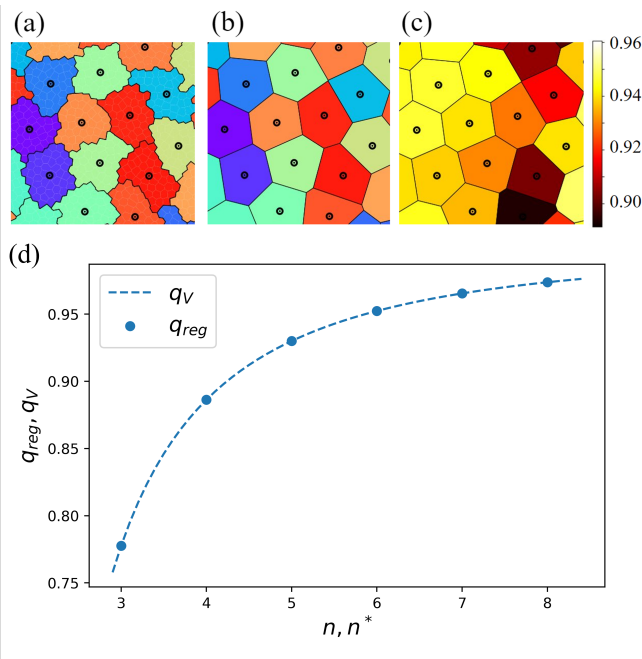


Figure 3. Using Voronoi tessellation to determine the shape index of lattice-based cells. (a) A snapshot of cells on the disordered lattice. The colors indicate individual cells and the black circles their centers of mass. (b) Voronoi tessellated version of the cells based on the position of the centers of mass. (c) Voronoi tessellated cells colored by their shape index q_v , as indicated by the color bar shown on the right-hand side. The data derives from a part of a simulation with $\alpha = 1.8$. (d) Isoperimetric quotient of regular polygons, $q_{reg}(n)$, as well as its generalization $q_v(n^*)$.

Third, we complement the hexatic-order analysis by

considering the dimensionless quantity called the *shape index*. For any 2D shape, this quantity is defined as P/\sqrt{A} , where P and A are the perimeter and the area, respectively. This parameter has been studied extensively in tissue mechanics, *e.g.*, see Refs. 18, 19, 23, 53, 106, 110, 128, 129. A slightly modified version of this quantity is the *isoperimetric quotient*, which is defined as $q = \sqrt{4\pi A}/P$. It is dimensionless as well, and equal to 1.0 for the circle, while being close to 0 for highly elongated shapes.

Here, we should note that the cell perimeter is not a well-defined quantity for lattice-based models like CPM. This is because the borders of the cells are defined by the edges of the lattice sites, which enforces excess jaggedness to the cells — in mathematical language, a natural metric to distance calculations. To overcome this issue, we applied Voronoi tessellation to the center-of-mass (CMS) positions of the cells. This enabled us to study the effective areas and perimeters of the generated polygons and compute the associated isoperimetric quotient. We use the subscript ‘V’, for example, q_v , to indicate the use of our Voronoi procedure. Figure 3 (a-c) shows a zoomed-in view of a snapshot that illustrates the process, as well as the obtained value of q_v . We should note that a correction was also introduced to evaluate the perimeter of the cells on the CPM [120, 121]. However, we chose to use Voronoi tessellation to make a clear comparison between this study and the vertex and Voronoi models that are being used in this context of epithelia.

The isoperimetric quotient of regular polygons with n edges, $q_{reg}(n)$, can be readily computed and reads

$$q_{reg}(n) = \frac{\sqrt{4\pi A_{reg}(1, n)}}{P_{reg}(1, n)} = \frac{\sqrt{2n\pi \sin(2\pi/n)}}{2n \sin(\pi/n)}, \quad (8)$$

where $A_{reg}(r, n)$ and $P_{reg}(r, n)$ are the area and the perimeter of a regular polygon having n edges and a circumscribing circle with radius r . This function maps the num-

ber of the edges of regular polygons to their isoperimetric quotient, and *vice versa*. We can now straightforwardly apply the right-hand side of Eq. (8) for non-integer values of n , which we call the *generalized edge number* and which we will identify using n^* . Numerically inverting this function, we uniquely obtain n^* for any given value of q_V . By doing so, we can assess the effective number of edges for a given (convex) cell shape. The dependence is shown in Fig. 3d.

Lastly, we also considered the *circularity* C of our model cells. This parameter was introduced by Zunic and Hirota [130, 131], and is calculated as follows. Given the area A of a 2D connected object, and the moment of inertia tensor \bar{I} , we write

$$C = \frac{1}{2\pi} \frac{A^2}{\bar{I}_{xx} + \bar{I}_{yy}}, \quad (9)$$

where in the denominator, the trace of the tensor is taken. Since the trace is invariant under translation and rotation, C is independent of the coordinate system. One should be careful in connection to Refs. 130 and 131, to note that people also use the term ‘circularity’ to refer to the quantity $4\pi A^2/P$, which is q^2 in our characterization. However, throughout this study, by circularity, we mean the quantity calculated by equation 9. This quantity is in fact, one of the Hu moment invariants [132] that are widely used in image processing and pattern recognition [133]. Circularity has also been used in studying cell morphology [134], branching patterns in organogenesis simulations [41], and pathological cell nucleus shape analysis [135]. However, to the best of our knowledge, thus far it has not been studied in the context of confluent tissue transitions. Similar to the isoperimetric quotient, we rely on a Voronoi tessellation to determine C_V . The circularity is much more strong nonlinear than q in the number of edges of a regular polygon. Therefore, we do *not* invert it to establish an equivalent circularity-derived generalized edge number n° .

III. Results

In this section, we introduce the main results of our CPM simulations. As explained in Section IIA, the control parameter in our simulations is α , which models the surface tension between cells. We start by showing that increasing α leads to a first-order phase transition from a disordered fluid to an ordered hexagonal phase on all lattices.

A. Hexatic Order and Diffusion

Figure 4 shows the (average) hexatic orientational order parameter $\langle |\psi_6| \rangle$ as a function of α and several representative snapshots of a part of the simulation area. The average hexatic order is generally an increasing function of α , except for high values of α on the square lattice, which we will return to shortly. For all our lattices there is a substantial increase in $\langle |\psi_6| \rangle$ in the range 0.7 to 0.8. This is indicative of a first-order phase transition from fluid to hexagonal solid – especially in the case of

a square lattice, where the transition is sharp⁶. This is confirmed by contrasting the first two columns of snapshots in Fig. 4b with each other. The centers of mass of the cells assume a hexagonal arrangement in the three subpanels. We also found coexistence between the disordered and ordered phases, see Fig.S1, further confirming the first-order nature of the transition. We will not concern ourselves with the existence of a potential intermediate hexatic phase here, but referencing the literature [113, 136, 137], it should be present.

Increasing α beyond the transition value, $\langle |\psi_6| \rangle \approx 0.75$ increases further. Our transition value is also comparable to that reported in Ref. 113. On a square lattice, it eventually assumes a maximum. We can appreciate the underlying cause of the high- α reduction by examining snapshot 7 in Fig. 4b. This reveals that for the square lattice, the cells become distorted into a *diamond* configuration with staircase-like borders. These are clearly lattice artifacts and this is further borne out by the sizable unphysical peak in the distribution of hexatic order, see Fig.S2. For the disordered lattice there is no such behavior; the distribution of hexatic order is smooth within the error.

We further characterized the behavior of our systems by examining the MSD scaling exponent β , as defined in Eq. (5). Figure 5a shows β for different lattices as a function of α . For low α , we obtain diffusive scaling $\beta = 1$ within the error, and the system is in a fluid-like state. Near the transition point, the exponent drops significantly and we observe subdiffusive dynamics in which, our model tissue behaves solid-like. The inset to Fig. 5a shows the effective diffusion coefficient D_{eff} for those regimes where $\beta > 0.95$. There is a substantial drop in diffusivity before crystallization, however, this is not indicative of glassy behavior as reported in other sources [53, 110, 111]; we will come back to this in Section IV.

Figure 5b shows β as a function of $\langle |\psi_6| \rangle$. This representation allows us to compare the onset of the subdiffusive dynamics for the three underlying lattices. As we have seen in Section II, the transition α has a grid sensitivity, due to the difference in the number of effective neighbors, which is eliminated in this representation. The square and irregular lattices appear to have similar onset points within the error, $\langle |\psi_6| \rangle \approx 0.7$. For the irregular lattice, we observe a slight elevation of β just before the onset point. This is explained by occasional flocking events by cells for α close to the transition value, which we observed. The transition value for the hexagonal lattice deviates from the other two and is localized at $\langle |\psi_6| \rangle \approx 0.76$. We believe that the inherent symmetry of the hexagonal lattice allows the cells to move around more readily in a diffusive manner, while already assuming a hexagonal configuration themselves. This demon-

⁶ Note that we work in the NVT ensemble and average over several realizations of the system, thereby washing out the coexistence.

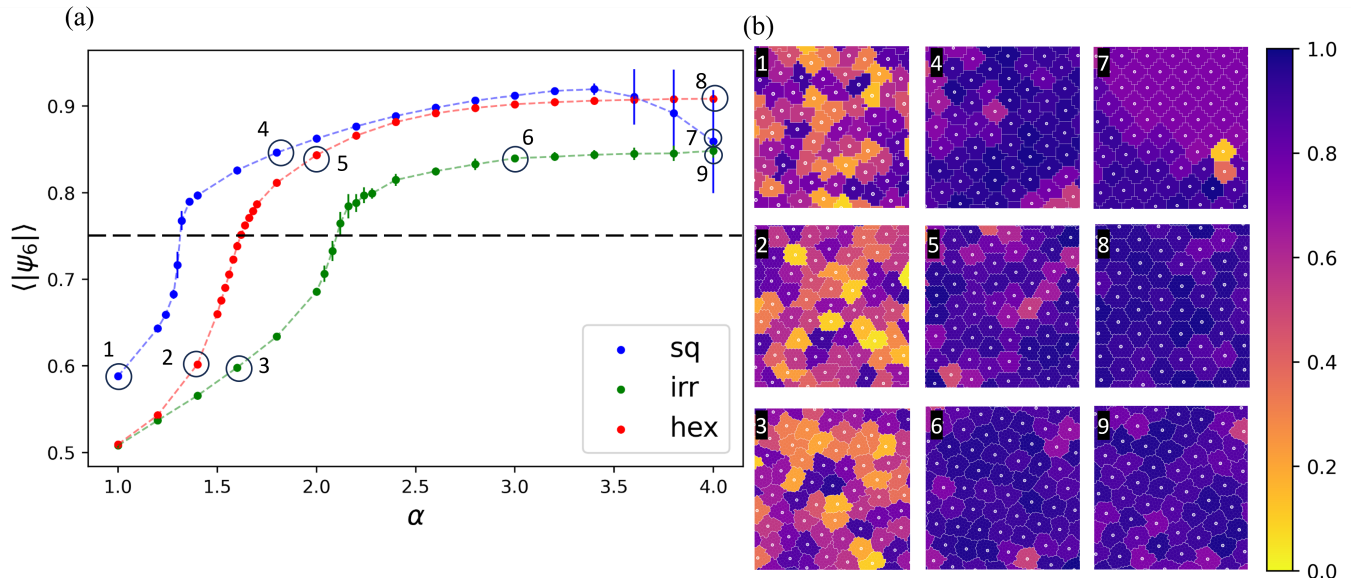


Figure 4. The formation of hexatic order on the three lattice types considered by increasing the surface tension. (a) The system-averaged hexatic order $\langle |\psi_6| \rangle$ as a function of α for the CPM on a square (blue), irregular (green), and hexagonal (red) lattice. The error bars show the standard error of the mean. The black dashed line indicates the transition value reported by Ref. 113. (b) Snapshots of the simulations specified by their labels in panel (a); only a small part of the simulation box is shown ($\sim 6\%$). The color of the cells indicate their local hexatic order.

strates that the symmetries of the underlying lattice can affect the behavior of the system near the fluid-to-solid transition.

B. Isoperimetric Quotient and Circularity

Figure 6a shows the equilibrium distribution of the Voronoi-based isoperimetric quotient, q_V , for two different values of α , obtained by using an irregular lattice. Because our model tissue is confluent, the q_V for the majority of the cells assumes values in the square-to-hexagon range. Note that for the fluid-like state, there is a dip in the value q_V around that of a regular pentagon. This is a consequence of the definition of q_V , rather than a profound result. Voronoi cells with 5 vertices always have values of $q_V \leq q_{\text{reg}}(5) = 0.930$, and cells with 6 vertices always have $q_V \leq q_{\text{reg}}(6) = 0.952$. However, whether a polygon with an arbitrary number of vertices m is pentagonal or hexagonal in nature, depends on whether its q_V is closer to $q_{\text{reg}}(5)$ or $q_{\text{reg}}(6)$, rather than the value of m . It is clear that upon undergoing a phase transition, the distribution shifts directly from being double-peaked to being strongly peaked close to a hexagonal value — another indicator of a first-order phase transition. The fact that the lattice is defect rich at high α in combination with the properties of q_V , makes it that the peak is not exactly centered about $q_V \approx 0.952$.

The distribution of q_V is insightful, but to help understand the properties of the underlying system, it is beneficial to convert it to an effective number of vertices n^* , see Fig. 6b and the definition in Section IID. The advantage of working directly with n^* , rather than q_V , is

that it allows us to examine the partition of the distribution. We identify the nearest integer number to a given n^* by $\lfloor n^* \rfloor$, which factors our range into distinct subsets of triangular, square, pentagonal, hexagonal, heptagonal, *etc.* neighborhoods. For example, all the cells having $\lfloor n^* \rfloor = 5$ (*i.e.*, $4.5 < n^* \leq 5.5$) can be referred to as *pseudo-pentagons*. Integrating the PDF belonging to the pseudo-pentagons provides insight into the fraction of pentagonal cells in the system. This includes cells with 5 or more edges, but for which some of the edges are very small.

Figure 7a shows fractions of pseudo-polygons f_{n^*} present in the system as a function of α . Interestingly, the curves for f_5 and f_6 show a crossover that matches well where we locate the phase transition based on our analysis of the long-time exponent β of the MSD. The physical intuition in this representation is clear: to crystallize, the system must have a majority of pseudo-hexagons. Figure 7b shows that this relation between the crossover and the transition is not limited to the irregular lattice. Here, we have plotted β as a function of f_6/f_5 ; when the ratio exceeds 1, the dynamics becomes subdiffusive. For the hexagonal lattice, the subdiffusive regime is assumed for higher values of the ratio, which is related to the fact that the hexagonal lattice favors the establishment of order over the reduction in model-cell diffusivity that is associated with it. The supplemental information goes into a longer discussion of the choice of this ratio, also considering the mean and median of the distribution. The latter also appears to be a good quantifier of the transition for these systems.

Returning to the data presented in Fig. 6, we see that

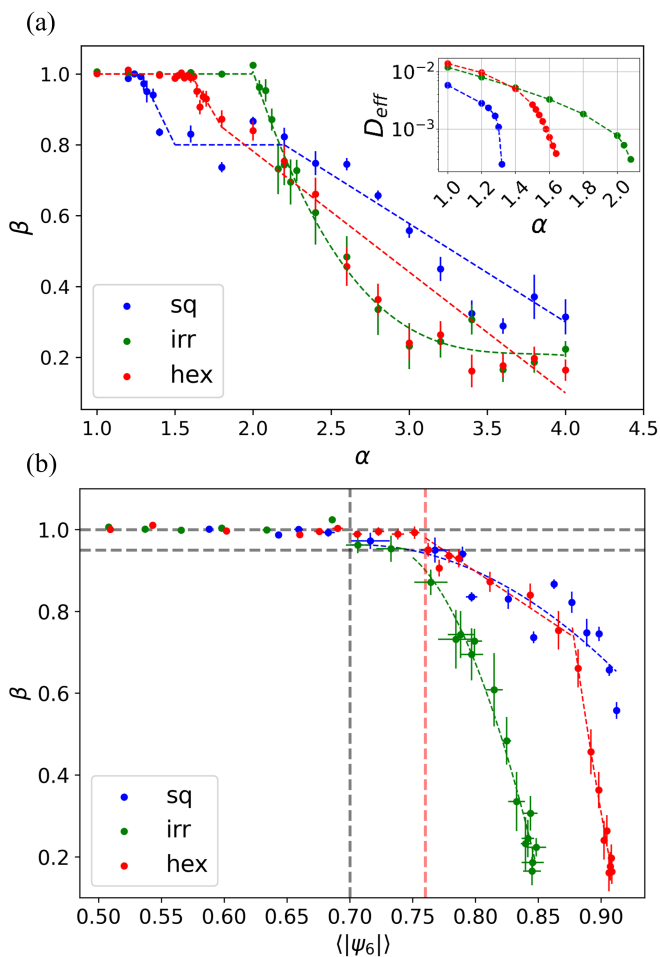


Figure 5. The long-time scaling of the mean-squared displacement (MSD) with the surface tension and the average hexatic order. (a) The power-law exponent of the long-time MSD β as a function of the interfacial energy α for the three different lattices as labeled. The dashed curves are a guide to the eye. The inset shows the effective diffusion coefficient D_{eff} as a function of α only for the data that has a sufficiently diffusive power-law ($\beta > 0.95$). (b) The exponent β as a function of the average hexatic order $\langle |\psi_6| \rangle$. The dashed red, green, and blue lines are guides to the eye, while the two dashed horizontal black lines indicates $\beta = 1$ and $\beta = 0.95$. The two vertical dashed lines indicate a transition in the β behavior, with the black line being representative of the square and irregular lattice, while the red line indicates the transition for the hexagonal lattice. In both panels, the error bars show the standard error of the mean.

the distributions pertaining to the fluid-like state (e.g., $\alpha = 1.8$) have two peaks, while the solid-like state (e.g., $\alpha = 2.2$) is characterized by a single peak. This statement holds in general and we can extract the positions of n^* for the maximum; or the two maxima and the local minimum, see Fig. 8. Similar data for the square and hexagonal lattices are provided in Fig.S5. We note that the behavior of the peak bears the hallmarks of a first-order phase transition, with a jump in the value of the ‘effective order parameter’ at $\alpha \approx 2.1$, as we alluded to

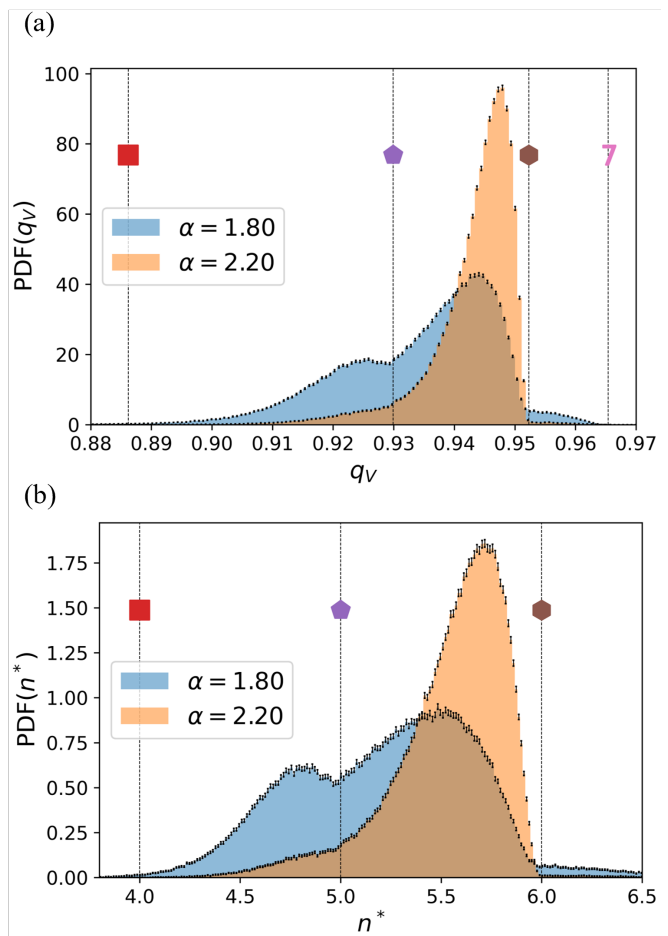


Figure 6. The distribution of Voronoi-based isoperimetric quotient q_V for a liquid- and solid-like state. (a) For a disordered lattice, we computed the probability density function (PDF) of q_V for $\alpha = 1.8$ (blue) and $\alpha = 2.2$ (orange), which are in the fluid and crystal states, respectively. (b) The same data, but now converted to an effective number of edges n^* . In both graphs, the error bars indicate the standard error of the mean, and values of q_V and n^* that correspond to regular polygons are indicated using dotted vertical lines and the use of symbols/numbers.

before. The minimum is effectively at $n^* = 5$, as is a feature of the definition of q_V . When the system transitions into the solid state, the peak reaches a nearly constant value of $n^* \approx 5.7$, which is shared among the studied underlying lattices. This is commensurate with the model cells transitioning to a state that is geometrically similar between the square, irregular, and hexagonal lattices. However, we emphasize that this does not imply that the transition is unaffected by the properties of the underlying lattice, as we have provided evidence for above.

Lastly, we calculated the circularity of the Voronoi-generated polygons for our model tissues. Figure 9a shows the distribution of C_V of the cells on the disordered lattice, for two values of α already considered in Fig. 6. It turns out that the distributions of C_V for all

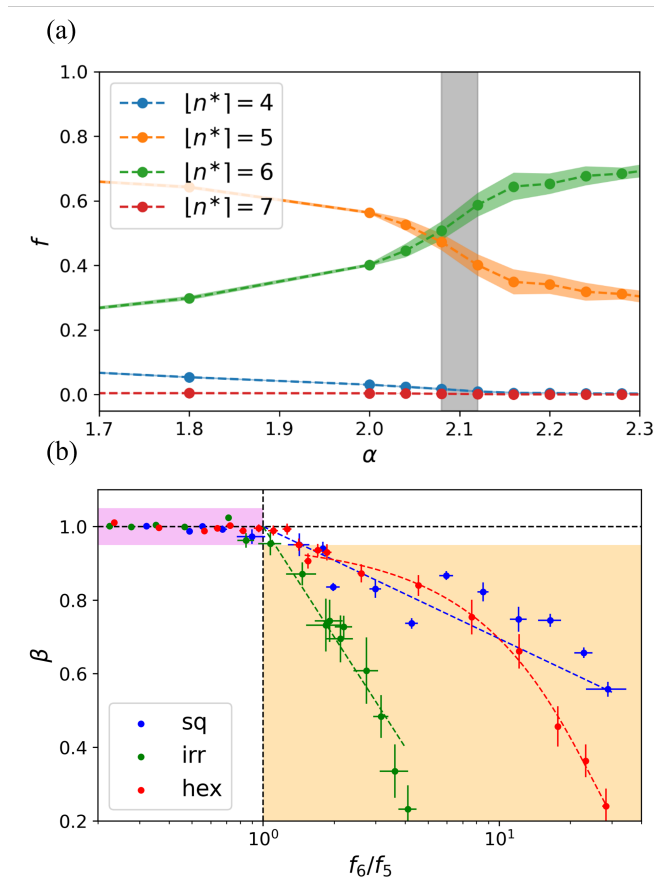


Figure 7. The trend in the fractions of pseudo-polygons can be used to determine the transition point. (a) The fractions of pseudo-polygons f_{n^*} as a function of the surface tension α obtained for a disordered lattice. The number of edges for the pseudo-polygons is indicated in the legend and the colored area around the respective curves indicates the standard error of the mean. The vertical gray bar shows the range for which the system transitions from a fluid to a hexagonal solid; the MSD exponent β drops below 0.95. (b) The exponent β as a function of the fractional ratio between pseudo-hexagons to the pseudo-pentagons f_6/f_5 . The violet and orange areas show the diffusive and the arrested regimes, respectively. The dashed lines are plotted to guide the eye. The error bars indicate the standard error of the mean.

the values of α studied here are unimodal, unlike those of q_V , *e.g.*, see figures 9 and S6. We also observe from our data that at the transition point, the mode of the distribution of C_V matches with the circularity of a regular pentagon, which we identify with $C(5)$. This relation is shown in Fig. 9b for the disordered lattice, where we show the long-time MSD exponent β as a function of the departure of the mode from the pentagonal value, *i.e.*, $\text{mode}(C_V) - C(5)$. It should be noted that the mode data presented here is complementary to the transition based on n^* for the isoperimetric quotient. Circularity compares the area with moment of inertia, rather than the perimeter.

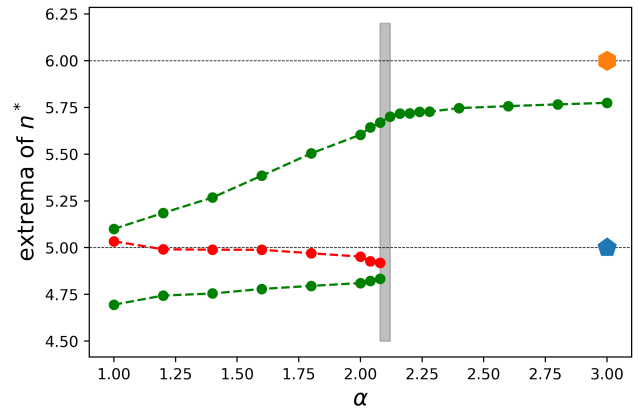


Figure 8. The fluid-to-solid transition in the model cell system as characterized using the extrema in the distribution of the Voronoi-based isoperimetric quotients. The n^* values for the local maxima are indicated in red and the local minimum in blue when it is present. The dashed lines are guides to the eye and the grey vertical bar indicates α interval in which we locate the transition, similar to Fig. 7a. The dotted horizontal lines indicate the values for a regular pentagon and hexagon, respectively, as labeled. The error bars are smaller than the point size. All data was obtained for a disordered lattice underlying the CPM dynamics.

IV. Discussion

In this section, we provide additional context to our research. We have split this into four parts for convenience. The first concerns itself with the quality of our phase diagram and the lack of a glassy phase. The second makes the connection to experimental observations to further justify the use of the CPM. The third provides insight into the efficiency of our algorithm and the challenges in working with an irregular-lattice CPM. We close with a larger discussion on the use of shape parameters.

A. The Phase Transition

On three different lattices studied here, we observed an order-disorder transition. This transition was reported previously for the square-lattice version of CPM [113], where it was studied as a function of temperature. Here, we show the transition as a function of the surface tension and show that it is not limited to the classical square-lattice version of CPM. By the Mermin-Wagner theorem, there should be a narrow, intermediate band of hexatic phase in the phase diagram, as also reported in the literature[113, 136, 137]. However, this phase is notoriously difficult to identify and we did not carry out the detailed analysis required to establish its presence. Our focus is instead on the effect of lattice artifacts on the overall trends.

Bearing this caveat in mind, our transitions have the hallmarks of a first-order phase transition. These include a sharp change in the value of the hexatic order and the presence of coexistence between ordered and disordered cell populations, as shown in figure S1. The value of

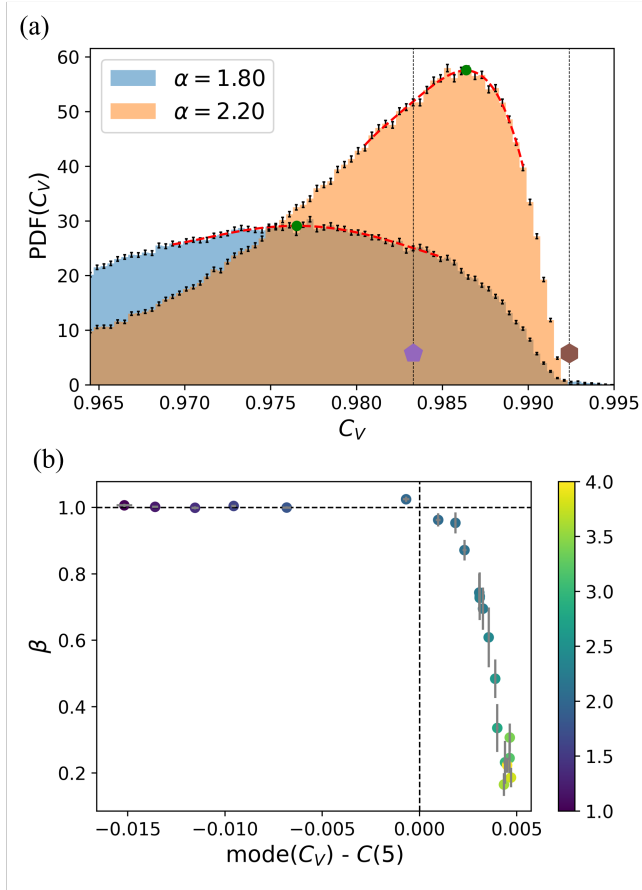


Figure 9. The circularity C_V of the Voronoi tessellation as an indicator of the phase transition. (a) The PDF of C_V for two different values of α on the disordered lattice. One is representative of the fluid-like regime ($\alpha = 2.0$, blue), and the other, of the solid-like regime ($\alpha = 2.2$, orange). The position of the peak of the distribution (green circles) is extracted from the red (polynomial) fits. The two dotted vertical lines and symbols indicate the value of circularity for a regular pentagon and hexagon, respectively. (b) The long-time exponent of the MSD, β , as a function of the departure between the mode of the distribution $\text{mode}(C_V)$ and the value of the circularity for a regular pentagon $C(5)$. The data points are colored by the value of α , as indicated in the color bar to the right. In both panels, the error bars show the standard error of the mean.

the isoperimetric quotient at the transition, see figure S4, lies between that of a regular pentagon and a regular hexagon, which is commensurate with this observation. Additionally, as is plotted in figure 4a, the transition value of hexatic order matches with the value reported in Ref. 113, providing additional support for the similarity between our findings and theirs. Other studies in the literature that used ‘deformable’ particles, *e.g.*, phase-field [60, 63] and Fourier contour [64] approaches, have also reported the emergence of hexagonal solid phases in model tissues, lending further credence to our result.

This makes the transition in the CPM markedly different from the jamming transitions reported for the ver-

tex [18, 106] and Voronoi models [53, 138]. These appear to leave the structure amorphous and occur at an average (target) value of $q = q_{\text{reg}}(5)$. The regular (perfect) pentagon is a shape that cannot tile the plane confluent. Thus, imposing this on all cells in the model tissue leads to frustration between local and global constraints, resulting in a disordered arrest. Considering the similarities between cellular-Potts, phase-field, and Fourier-contour models, we surmise that a lack of border flexibility may be partly responsible for the difference. That is, in the vertex and Voronoi descriptions, the cells are described as polygons whose dynamics is ruled by their vertices and centroids, respectively. This means that they have far fewer degrees of freedom to their dynamics when compared to CPM at an equal cell number.

In this context, the work by Sadhukhan and Nandi [111] should be mentioned, who have reported glassy behavior in the CPM with a Hamiltonian restricting the perimeter of the cells, as well as their area. This choice brings their version of CPM closer to the vertex and Voronoi models. However, we believe that the observation of square cells by these authors may be attributed to lattice artifacts [36]. For their large preferred perimeter regime, the *interlocking* of cells can also be attributed to the underlying lattice. As a lattice-based model, CPM has the inherent weakness of dealing with target perimeter lengths. Our work most closely follows that of Chiang and Marenduzzo [110] who identify a glass transition for the square-lattice CPM. However, in reproducing their results, we have conclusively shown that this glassy behavior is not present. Lastly, we turn to the results of Ref. 112. They report a similar value of the shape parameter at the transition. However, they identify this transition as a jamming one. This is likely a misinterpretation of their findings, and this issue could be resolved by examining the hexatic order in their ‘jammed’ phase.

B. Connection to Experiment

There have been many studies focused on jamming transitions and glassy behavior in living tissues, *e.g.*, reviewed by Refs. 15, 103. However, these are not the only arrested patterns that can exist in these systems. Hexagonally packed cell arrangements are also frequently found in epithelia across a range of species and developmental stages [139–155]. Although more complicated mechanisms such as adherens junctions [156] can play a role in maintaining cellular order in hexagonal cell packings, it is informative to distinguish models that can capture this type of packing by their nature. These models, such as the ir(regular) versions of CPM, have the potential as a computational framework to study hexagonally ordered biological systems.

C. Resolving lattice artifacts

The main advantage we derive from our irregular underlying lattice is to rid our simulations of obvious lattice artifacts, without having to resort to higher-order neighbor coupling, as has been discussed in, *e.g.*, Ref. 36. Figures 4 and S2 both clearly evidence that a square lattice

CPM with a Moore neighborhood rule can lead to an abnormal distribution of hexatic order at high surface tension. There are lattice artifacts on the hexagonal lattice too, although they are not as visually apparent as they are on the square lattice. The inherent symmetry of the hexagonal lattice can facilitate the orientational order of the cells, while the cells can still diffusively move around as particles in a fluid. This can be understood from the slight, but observable, mismatch between the onset of arrested dynamics on hexagonal and two other lattices, seen in Figures 5b and 7b. The disordered lattice is free of both of these artifacts within the error. It predicts the transition value of the hexatic order equal to that found for the square lattice while showing smooth (physical) distributions for this quantity at any value of surface tension. This is an important advantage because as is discussed in several studies [19, 138, 157–159], the shape of the cells can be strongly connected to the dynamics of the tissue.

D. Efficiency and Considerations

Our irregular-lattice version of CPM not only is free of demonstrable artifacts but it can also be applied to any lattice that derives from a Voronoi construction, including regular ones. This provides our description with greater flexibility. In fact, for simulations on the hexagonal lattice, we used the same code, but with a perfect hexagonal Voronoi lattice as an input. When using an irregular lattice, it may be prudent to generate several independent realizations of the lattice. This should further reduce the correlations when taking statistical averages.

In terms of computational efficiency, an extra run time is incurred using our approach compared to the square-lattice CPM. This was, however, very reasonable, as the average simulation time per 10^6 MC sweeps for the square-lattice CPM was generally in the range of 7 to 11 hours, while it was in the range of 8 to 15 hours for our generalized CPM. This timing data was obtained using cluster nodes equipped with, on average, 20 CPU cores and 64 GB of RAM. Even in the worst case, the run time was less than twice that of the regular CPM.

Note that to properly evaluate the perimeter of our cells, we used Voronoi tessellation on their centers of mass. Even on the irregular lattice, the contour length of the cells is artificially high, as we established by examining a very large circular cell in isolation. This is a limitation of the model, which could be overcome by using alternative perimeter evaluation algorithms such as Voronoi tessellation.

E. Shape-Parameter-Based Characterization

Several studies have looked at distributions of properties of the cell neighborhood. Some considered the aspect ratio of the cells [138, 160], while others extracted the number of neighbors [49, 153, 161, 162]. Here, we calculated the distribution underlying the mean isoperimetric quotient, and from these, we extracted fractions of pseudo- n^* -gons to gain a deeper insight into the system. Figure 7 for the irregular and figure S3 for the reg-

ular lattices, respectively, show that the majority of the polygons in the subdiffusive state are pseudo-hexagons, while in the fluid-like regime they are pseudo-pentagons. At the transition, we have observed that their relative abundance in the sample crosses over.

We found a single study by Saito and Ishihara [64], who examined isoperimetric-quotient distributions across the transition in their Fourier-contour model. They also reported a unimodal-to-bimodal transition in the distributions, as we have observed. The bimodality in the fluid-like regime is indicative of a coexistence between more-rounded and less-rounded cells, which is understood to lead to fluidity of the tissue. We note that in the current literature [60, 64, 110–112, 163] there is a tendency to focus on the mean value of the shape parameter as the indicator of transition. This is undoubtedly motivated by its relevance to the behavior of the vertex and Voronoi models [18, 20, 53–55, 106, 128, 138, 164–167]. However, as we have argued above, these models fall into a different class. We, therefore, believe it to be informative in general to examine shape-parameter distributions rather than only means.

As a complementary quantity to describe the shape of the cells we studied the circularity parameter C [130, 131], which is in essence, one of Hu moment invariants [132]. This compares the area of shapes to their moment of inertia, rather than to their perimeter, which is the case for q . This makes C less sensitive to noise at the boundary or definition issues with perimeter length. That is, we could have performed the circularity analysis on the original cell shapes rather than their Voronoi-based counterparts. However, we found that applying Voronoi tessellation to the cells led to a better comparison between the two roundness measures.

V. Summary and Outlook

In this study, we extended the regular (square-lattice) cellular Potts model to work on arbitrary (ir)regular lattices. The main motivation of this study was to eliminate lattice artifacts observed for square-lattice CPMs in the literature. We demonstrated that such artifacts could indeed be eliminated by using an irregular lattice generated from a fluid-like state using Voronoi tessellation. Our generalized CPM maintains many of the desirable features of a base CPM, at the price of a small computational overhead.

We gained the following insights using our algorithm on both irregular, square, and hexagonal lattices. First, there is an order-disorder transition in confluent cell monolayers when using CPM on all lattices that we considered. This sets the base CPM apart from the Voronoi and vertex models, which report a transition characterized by arrested dynamics for which the structure remains disordered. This makes CPM suited to describe epithelia in which ordered cell arrangements form. Second, for the square lattice, the cell shape can be impacted by artifacts above the transition, while for the hexagonal

lattice, the fluidity of the tissue remains oddly high. Our irregular-lattice CPM did not exhibit these undesirable features.

In addition, we gained deeper insight into the transition by studying the distributions of different order parameters across the transition. This included the hexatic bond order, the isoperimetric quotient, and the circularity, which overlap in their descriptiveness of local neighborhoods. For the isoperimetric quotient, the transition is closely correlated to the crossover in the fraction of pentagonal and hexagonal neighborhoods found in our simulations. However, the transition does not lie at an average isoperimetric quotient of a pentagon, as is the case for the vertex and Voronoi models. This is because, unlike these two systems, the shape is not a target parameter in the Hamiltonian describing the system. It is further important to realize that examining the mean isoperimetric quotient, or the related shape index, may give an incomplete picture of the behavior of the system.

Looking forward, we note that artifacts can be straightforwardly eliminated through the introduction of an irregular grid. This may have additional advantages when coupling the dynamics of the cells to that of external fields, such as food or chemical fields in bacterial colonies [168]. We will explore these directions in modeling real biological tissues using our generalized CPM in the future and hope this will lead to wider adoption of

our approach.

Data Availability

Open data package containing the means to reproduce the results of the simulations available at: [DOI to be inserted]

Author Contributions

The authors contributed as follows to the study: Conceptualization (JdG & HN), Data Curation (HN), Formal Analysis (HN), Funding Acquisition (JdG), Investigation (HN), Methodology (JdG & HN), Project Administration (JdG), Resources (JdG), Software (HN), Supervision (JdG), Validation (HN & JdG), Visualization (HN), Writing – Original Draft (HN), Writing – Review & Editing (JdG).

Conflicts of interest

The authors declare that there are no conflicts of interest.

Acknowledgements

The authors acknowledge financial support from the Netherlands Organization for Scientific Research (NWO) through Start-Up Grant 740.018.013. We are grateful to Bryan Verhoef, Kim William Torre, Meike Bos, and Davide Marenduzzo for useful discussions.

-
- [1] M. Merkel and M. L. Manning, Using cell deformation and motion to predict forces and collective behavior in morphogenesis, *Semin. Cell Dev. Biol. Extracellular Vesicles*, **67**, 161 (2017).
- [2] S.-Z. Lin, S. Ye, G.-K. Xu, B. Li, and X.-Q. Feng, Dynamic Migration Modes of Collective Cells, *Biophys. J.* **115**, 1826 (2018).
- [3] M. Akiyama, T. Sushida, S. Ishida, and H. Haga, Mathematical model of collective cell migrations based on cell polarity, *Dev. Growth Differ.* **59**, 471 (2017), eprint: <https://onlinelibrary.wiley.com/doi/pdf/10.1111/dgd.12381>.
- [4] P. Friedl and D. Gilmour, Collective cell migration in morphogenesis, regeneration and cancer, *Nat. Rev. Mol. Cell Biol.* **10**, 445–457 (2009).
- [5] P. Rørth, Collective Cell Migration, *Annu. Rev. Cell Dev. Biol.* **25**, 407 (2009).
- [6] M. P. De Leon, F.-L. Wen, G. J. Paylaga, Y.-T. Wang, H.-Y. Roan, C.-H. Wang, C.-D. Hsiao, K.-H. Lin, and C.-H. Chen, Mechanical waves identify the amputation position during wound healing in the amputated zebrafish tailfin, *Nat. Phys.*, **1** (2023), publisher: Nature Publishing Group.
- [7] H. Xu, Y. Huo, Q. Zhou, L. A. Wang, P. Cai, B. Doss, C. Huang, and K. J. Hsia, Geometry-mediated bridging drives nonadhesive stripe wound healing, *Proc. Natl. Acad. Sci. U.S.A.* **120**, e2221040120 (2023), publisher: Proceedings of the National Academy of Sciences.
- [8] A. Brugués, E. Anon, V. Conte, J. H. Veldhuis, M. Gupta, J. Colombelli, J. J. Muñoz, G. W. Brodland, B. Ladoux, and X. Trepat, Forces driving epithelial wound healing, *Nat. Phys.* **10**, 683 (2014), publisher: Nature Publishing Group.
- [9] M. Poujade, E. Grasland-Mongrain, A. Hertzog, J. Jouanneau, P. Chavrier, B. Ladoux, A. Buguin, and P. Silberzan, Collective migration of an epithelial monolayer in response to a model wound, *Proc. Natl. Acad. Sci. U.S.A.* **104**, 15988 (2007), publisher: Proceedings of the National Academy of Sciences.
- [10] K. J. Cheung, E. Gabrielson, Z. Werb, and A. J. Ewald, Collective Invasion in Breast Cancer Requires a Conserved Basal Epithelial Program, *Cell* **155**, 1639 (2013).
- [11] J. Metzcar, Y. Wang, R. Heiland, and P. Macklin, A Review of Cell-Based Computational Modeling in Cancer Biology, *JCO Clin. Cancer Inform.*, **1** (2019), publisher: Wolters Kluwer.
- [12] O. Ilina, P. G. Gritsenko, S. Syga, J. Lippoldt, C. A. M. La Porta, O. Chepizhko, S. Grosser, M. Vullings, G.-J. Bakker, J. Starruß, P. Bult, S. Zapperi, J. A. Käs, A. Deutsch, and P. Friedl, Cell-cell adhesion and 3d matrix confinement determine jamming transitions in breast cancer invasion, *Nat. Cell Biol.* **22**, 1103–1115 (2020).
- [13] S. Grosser, J. Lippoldt, L. Oswald, M. Merkel, D. M. Sussman, F. Renner, P. Gottheil, E. W. Morawetz, T. Fuhs, X. Xie, S. Pawlizak, A. W. Fritsch, B. Wolf, L.-C. Horn, S. Briest, B. Aktas, M. L. Manning, and J. A. Käs, Cell and nucleus shape as an indicator of tissue fluidity in carcinoma, *Phys. Rev. X* **11**, 011033 (2021).
- [14] L. Oswald, S. Grosser, D. M. Smith, and J. A. Käs, Jamming transitions in cancer, *J. Phys. D: Appl. Phys.* **50**,

- 483001 (2017).
- [15] E. Blauth, H. Kubitschke, P. Gottheil, S. Grosser, and J. A. Käs, Jamming in embryogenesis and cancer progression, *Front. Phys.* **9**, 666709 (2021).
- [16] X. Yin, Y.-Q. Liu, L.-Y. Zhang, D. Liang, and G.-K. Xu, Emergence, pattern, and frequency of spontaneous waves in spreading epithelial monolayers, *Nano Letters* **24**, 3631–3637 (2024).
- [17] J.-M. Armengol-Collado, L. N. Carenza, J. Eckert, D. Krommydas, and L. Giomi, Epithelia are multiscale active liquid crystals, *Nat. Phys.* , 1 (2023), publisher: Nature Publishing Group.
- [18] D. Bi, J. H. Lopez, J. M. Schwarz, and M. L. Manning, A density-independent rigidity transition in biological tissues, *Nat. Phys.* **11**, 1074–1079 (2015).
- [19] J.-A. Park, J. H. Kim, D. Bi, J. A. Mitchel, N. T. Qazvini, K. Tantisira, C. Y. Park, M. McGill, S.-H. Kim, B. Gweon, J. Notbohm, R. Steward Jr, S. Burger, S. H. Randell, A. T. Kho, D. T. Tambe, C. Hardin, S. A. Shore, E. Israel, D. A. Weitz, D. J. Tschumperlin, E. P. Henske, S. T. Weiss, M. L. Manning, J. P. Butler, J. M. Drazen, and J. J. Fredberg, Unjamming and cell shape in the asthmatic airway epithelium, *Nat. Mater.* **14**, 1040–1048 (2015).
- [20] O. K. Damavandi, E. Lawson-Keister, and M. L. Manning, Universal features of rigidity transitions in vertex models for biological tissues (2022).
- [21] A. Hopkins, M. Chiang, B. Loewe, D. Marenduzzo, and M. C. Marchetti, Local Yield and Compliance in Active Cell Monolayers, *Phys. Rev. Lett.* **129**, 148101 (2022), publisher: American Physical Society.
- [22] S. M. Fielding, J. O. Cochran, J. Huang, D. Bi, and M. C. Marchetti, Constitutive model for the rheology of biological tissue, *Phys. Rev. E* **108**, L042602 (2023), publisher: American Physical Society.
- [23] M. J. Hertaeg, S. M. Fielding, and D. Bi, Discontinuous shear thickening in biological tissue rheology, *Phys. Rev. X* **14**, 011027 (2024).
- [24] A. Chamoli, A. S. Gosavi, U. P. Shirwadkar, K. V. Wangdale, S. K. Behera, N. K. Kurrey, K. Kalia, and A. Mandoli, Overview of oral cavity squamous cell carcinoma: Risk factors, mechanisms, and diagnostics, *Oral Oncol.* **121**, 105451 (2021).
- [25] C. Levra Levron, L. Elettrico, C. Duval, G. Piacenti, V. Proserpio, and G. Donati, Bridging tissue repair and epithelial carcinogenesis: epigenetic memory and field cancerization, *Cell Death Differ.* , 1 (2024), publisher: Nature Publishing Group.
- [26] R. Okamoto and M. Watanabe, Role of epithelial cells in the pathogenesis and treatment of inflammatory bowel disease, *J. Gastroenterol.* **51**, 11 (2016).
- [27] M. J. Holtzman, D. E. Byers, J. Alexander-Brett, and X. Wang, The role of airway epithelial cells and innate immune cells in chronic respiratory disease, *Nat. Rev. Immunol.* **14**, 686 (2014), publisher: Nature Publishing Group.
- [28] A. K. Klettner and S. Dithmar, eds., *Retinal Pigment Epithelium in Health and Disease* (Springer International Publishing, Cham, 2020) pp. 117–185.
- [29] I. T. Stancil, J. E. Michalski, D. Davis-Hall, H. W. Chu, J.-A. Park, C. M. Magin, I. V. Yang, B. J. Smith, E. Dobrinskikh, and D. A. Schwartz, Pulmonary fibrosis distal airway epithelia are dynamically and structurally dysfunctional, *Nat. Commun.* **12**, 4566 (2021), publisher: Nature Publishing Group.
- [30] R. Alert and X. Trepat, Physical models of collective cell migration, *Annu. Rev. Condens. Matter Phys.* **11**, 77–101 (2020).
- [31] B. A. Camley and W.-J. Rappel, Physical models of collective cell motility: from cell to tissue, *J. Phys. D: Appl. Phys.* **50**, 113002 (2017), publisher: IOP Publishing.
- [32] M. R. Shaebani, A. Wysocki, R. G. Winkler, G. Gompper, and H. Rieger, Computational models for active matter, *Nat. Rev. Phys.* **2**, 181 (2020), number: 4 Publisher: Nature Publishing Group.
- [33] F. Graner and J. A. Glazier, Simulation of biological cell sorting using a two-dimensional extended potts model, *Phys. Rev. Lett.* **69**, 2013–2016 (1992).
- [34] M. Scianna and L. Preziosi, *Cellular Potts models*, Chapman & Hall/CRC Mathematical and Computational Biology (CRC Press, Boca Raton, FL, 2013).
- [35] M. Scianna and L. Preziosi, Multiscale developments of the cellular potts model, *Multiscale Modeling & Simulation* **10**, 342–382 (2012).
- [36] A. F. M. Marée, V. A. Grieneisen, and P. Hogeweg, The cellular potts model and biophysical properties of cells, tissues and morphogenesis, in *Single-Cell-Based Models in Biology and Medicine*, edited by A. R. A. Anderson, M. A. J. Chaplain, and K. A. Rejniak (Birkhäuser Basel, Basel, 2007) pp. 107–136.
- [37] A. Szabó and R. M. H. Merks, Cellular potts modeling of tumor growth, tumor invasion, and tumor evolution, *Front. Oncol.* **3**, 87 (2013).
- [38] T. Hirashima, E. G. Rens, and R. M. H. Merks, Cellular potts modeling of complex multicellular behaviors in tissue morphogenesis, *Dev. Growth Differ.* **59**, 329–339 (2017).
- [39] S. E. M. Boas, Y. Jiang, R. M. H. Merks, S. A. Prokopiou, and E. G. Rens, Cellular potts model: Applications to vasculogenesis and angiogenesis, in *Probabilistic Cellular Automata* (Springer International Publishing, 2018) p. 279–310.
- [40] P. HOGEWEG, Evolving mechanisms of morphogenesis: on the interplay between differential adhesion and cell differentiation, *J. Theor. Biol.* **203**, 317–333 (2000).
- [41] A. Poorkhanalikhoudehi and K.-H. Zimmermann, Cellular automaton for kidney branching morphogenesis, *WSEAS TRANSACTIONS ON BIOLOGY AND BIOMEDICINE* **18**, 170–182 (2021).
- [42] G. B. Ermentrout and L. Edelstein-Keshet, Cellular Automata Approaches to Biological Modeling, *J. Theor. Biol.* **160**, 97 (1993).
- [43] H. Hatzikirou and A. Deutsch, Cellular Automata as Microscopic Models of Cell Migration in Heterogeneous Environments, in *Current Topics in Developmental Biology, Multiscale Modeling of Developmental Systems*, Vol. 81, edited by S. Schnell, P. K. Maini, S. A. Newman, and T. J. Newman (Academic Press, 2008) pp. 401–434.
- [44] J. M. Nava-Sedeño, H. Hatzikirou, F. Peruani, and A. Deutsch, Extracting cellular automaton rules from physical Langevin equation models for single and collective cell migration, *J. Math. Biol.* **75**, 1075 (2017).
- [45] Z. Kirchner, A. Geohagan, and A. Truszkowska, A Vicsek-type model of confined cancer cells with variable clustering affinities, *Integr. Biol.* **16**, zya005 (2024).
- [46] B. A. Camley, J. Zimmermann, H. Levine, and W.-J. Rappel, Collective Signal Processing in Cluster Chemotaxis: Roles of Adaptation, Amplification, and Co-attraction in Collective Guidance, *PLOS Comput. Biol.* **12**, e1005008

- (2016), publisher: Public Library of Science.
- [47] M. Basan, J. Elgeti, E. Hannezo, W.-J. Rappel, and H. Levine, Alignment of cellular motility forces with tissue flow as a mechanism for efficient wound healing, *Proc. Natl. Acad. Sci. U.S.A.* **110**, 2452 (2013), publisher: Proceedings of the National Academy of Sciences.
- [48] M. Campo, S. K. Schnyder, J. J. Molina, T. Speck, and R. Yamamoto, Spontaneous spatiotemporal ordering of shape oscillations enhances cell migration, *Soft Matter* **15**, 4939 (2019), publisher: The Royal Society of Chemistry.
- [49] R. Farhadifar, J.-C. Röper, B. Aigouy, S. Eaton, and F. Jülicher, The influence of cell mechanics, cell-cell interactions, and proliferation on epithelial packing, *Curr. Biol.* **17**, 2095–2104 (2007).
- [50] S. Alt, P. Ganguly, and G. Salbreux, Vertex models: From cell mechanics to tissue morphogenesis, *Philos. Trans. R. Soc. B* **372**, 20150520 (2017).
- [51] A. G. Fletcher, M. Osterfield, R. E. Baker, and S. Y. Shvartsman, Vertex Models of Epithelial Morphogenesis, *Biophys. J.* **106**, 2291 (2014).
- [52] K. Landsberg, R. Farhadifar, J. Ranft, D. Umetsu, T. Widmann, T. Bittig, A. Said, F. Jülicher, and C. Dahmann, Increased Cell Bond Tension Governs Cell Sorting at the *Drosophila* Anteroposterior Compartment Boundary, *Curr. Biol.* **19**, 1950 (2009).
- [53] D. Bi, X. Yang, M. C. Marchetti, and M. L. Manning, Motility-driven glass and jamming transitions in biological tissues, *Phys. Rev. X* **6**, 021011 (2016).
- [54] F. Giavazzi, M. Paoluzzi, M. Macchi, D. Bi, G. Scita, M. L. Manning, R. Cerbino, and M. C. Marchetti, Flocking transitions in confluent tissues, *Soft Matter* **14**, 3471–3477 (2018).
- [55] X. Yang, D. Bi, M. Czajkowski, M. Merkel, M. L. Manning, and M. C. Marchetti, Correlating cell shape and cellular stress in motile confluent tissues, *Proc. Natl. Acad. Sci. U.S.A.* **114**, 12663–12668 (2017).
- [56] D. E. P. Pinto, M. M. T. da Gama, and N. A. M. Araújo, Cell motility in confluent tissues induced by substrate disorder, *Phys. Rev. Res.* **4**, 023186 (2022), publisher: American Physical Society.
- [57] A. Moure and H. Gomez, Phase-Field Modeling of Individual and Collective Cell Migration, *Arch. Comput. Methods Eng.* **28**, 311 (2021).
- [58] G. Zhang and J. M. Yeomans, Active Forces in Confluent Cell Monolayers, *Phys. Rev. Lett.* **130**, 038202 (2023), publisher: American Physical Society.
- [59] M. Nonomura, Study on Multicellular Systems Using a Phase Field Model, *PLOS ONE* **7**, e33501 (2012), publisher: Public Library of Science.
- [60] B. Loewe, M. Chiang, D. Marenduzzo, and M. C. Marchetti, Solid-Liquid Transition of Deformable and Overlapping Active Particles, *Phys. Rev. Lett.* **125**, 038003 (2020), publisher: American Physical Society.
- [61] H. P. Jain, A. Voigt, and L. Angheluta, Robust statistical properties of T1 transitions in a multi-phase field model of cell monolayers, *Sci. Rep.* **13**, 10096 (2023), publisher: Nature Publishing Group.
- [62] D. Wenzel and A. Voigt, Multiphase field models for collective cell migration, *Phys. Rev. E* **104**, 054410 (2021), publisher: American Physical Society.
- [63] S. Monfared, G. Ravichandran, J. Andrade, and A. Doostmohammadi, Mechanical basis and topological routes to cell elimination, *eLife* **12**, e82435 (2023).
- [64] N. Saito and S. Ishihara, Active deformable cells undergo cell shape transition associated with percolation of topological defects (2023), arXiv:2303.03580 [q-bio.TO].
- [65] J. Tkadlec, K. Kaveh, K. Chatterjee, and M. A. Nowak, Evolutionary dynamics of mutants that modify population structure, *J. R. Soc. Interface* **20**, 20230355 (2023), publisher: Royal Society.
- [66] H. Nemati, K. Kaveh, and M. R. Ejtehadi, Counterintuitive properties of evolutionary measures: A stochastic process study in cyclic population structures with periodic environments, *J. Theor. Biol.* **564**, 111436 (2023).
- [67] J. Renton and K. M. Page, Cooperative success in epithelial public goods games, *J. Theor. Biol.* **528**, 110838 (2021).
- [68] J. Renton and K. M. Page, Evolution of cooperation in an epithelium, *J. R. Soc. Interface* **16**, 20180918 (2019), publisher: Royal Society.
- [69] V. S. K. Manem, K. Kaveh, M. Kohandel, and S. Sivaloganathan, Modeling Invasion Dynamics with Spatial Random-Fitness Due to Micro-Environment, *PLOS ONE* **10**, e0140234 (2015), publisher: Public Library of Science.
- [70] A. Goriely, *The Mathematics and Mechanics of Biological Growth*, Interdisciplinary Applied Mathematics, Vol. 45 (Springer New York, New York, NY, 2017) pp. 51–59.
- [71] C. Beatrice, C. Kirch, S. Henkes, F. Graner, and L. G. Brunnet, Discriminating between individual-based models of collective cell motion in a benchmark flow geometry using standardised spatiotemporal patterns, *Soft Matter* 10.1039/D3SM00187C (2023), publisher: The Royal Society of Chemistry.
- [72] J. M. Osborne, A. G. Fletcher, J. M. Pitt-Francis, P. K. Maini, and D. J. Gavaghan, Comparing individual-based approaches to modelling the self-organization of multicellular tissues, *PLOS Comput. Biol.* **13**, e1005387 (2017), publisher: Public Library of Science.
- [73] J. A. Glazier and F. Graner, Simulation of the differential adhesion driven rearrangement of biological cells, *Phys. Rev. E* **47**, 2128–2154 (1993).
- [74] J. C. M. Mombach, J. A. Glazier, R. C. Raphael, and M. Zajac, Quantitative comparison between differential adhesion models and cell sorting in the presence and absence of fluctuations, *Phys. Rev. Lett.* **75**, 2244–2247 (1995).
- [75] R. Z. Tan, The effects of cellular interactions on the sizes, composition, and dynamics of migrating cancer cell clusters, *J. Comput. Sci.* **76**, 102237 (2024).
- [76] G. Y. Ouaknin and P. Z. Bar-Yoseph, Stochastic collective movement of cells and fingering morphology: no maverick cells, *Biophys. J.* **97**, 1811 (2009).
- [77] J. Käfer, P. Hogeweg, and A. F. M. Marée, Moving Forward Moving Backward: Directional Sorting of Chemotactic Cells due to Size and Adhesion Differences, *PLOS Comput. Biol.* **2**, e56 (2006), publisher: Public Library of Science.
- [78] L. v. Steijn, J. A. J. Wondergem, K. Schakenraad, D. Heinrich, and R. M. H. Merks, Deformability and collision-induced reorientation enhance cell topotaxis in dense microenvironments, *Biophys. J.* **122**, 2791 (2023), publisher: Elsevier.
- [79] L. Plazen, J. A. Rahbani, C. M. Brown, and A. Khadra, Polarity and mixed-mode oscillations may underlie different patterns of cellular migration, *Sci. Rep.* **13**, 4223 (2023), publisher: Nature Publishing Group.

- [80] I. M. N. Wortel, I. Niculescu, P. M. Koliijn, N. S. Gov, R. J. de Boer, and J. Textor, Local actin dynamics couple speed and persistence in a cellular Potts model of cell migration, *Biophys. J.* **120**, 2609 (2021).
- [81] I. Niculescu, J. Textor, and R. J. de Boer, Crawling and Gliding: A Computational Model for Shape-Driven Cell Migration, *PLOS Comput. Biol.* **11**, e1004280 (2015).
- [82] K. Matsushita, H. Hashimura, H. Kuwayama, and K. Fujimoto, Collective Cell Movement under Cell-Scale Tension Gradient at Tissue Interface, *J. Phys. Soc. Jpn.* **91**, 054802 (2022), publisher: The Physical Society of Japan.
- [83] A. J. Kabla, Collective cell migration: leadership, invasion and segregation, *J. R. Soc. Interface* **9**, 3268 (2012).
- [84] A. R. Noppe, A. P. Roberts, A. S. Yap, G. A. Gomez, and Z. Neufeld, Modelling wound closure in an epithelial cell sheet using the cellular Potts model, *Integr. Biol.* **7**, 1253 (2015).
- [85] M. Scianna, An extended Cellular Potts Model analyzing a wound healing assay, *Comput. Biol. Med.* **62**, 33 (2015).
- [86] B. M. Rubenstein and L. J. Kaufman, The Role of Extracellular Matrix in Glioma Invasion: A Cellular Potts Model Approach, *Biophys. J.* **95**, 5661 (2008), publisher: Elsevier.
- [87] E. Tsingos, B. H. Bakker, K. A. E. Keijzer, H. J. Hupkes, and R. M. H. Merks, Hybrid cellular Potts and bead-spring modeling of cells in fibrous extracellular matrix, *Biophys. J.* **122**, 2609 (2023), publisher: Elsevier.
- [88] R. M. Crossley, S. Johnson, E. Tsingos, Z. Bell, M. Berardi, M. Botticelli, Q. J. S. Braat, J. Metzcar, M. Ruscone, Y. Yin, and R. Shuttleworth, Modeling the extracellular matrix in cell migration and morphogenesis: a guide for the curious biologist, *Front. Cell Dev. Biol.* **12** (2024), publisher: Frontiers.
- [89] M. H. Swat, G. L. Thomas, J. M. Belmonte, A. Shirinifard, D. Hmeljak, and J. A. Glazier, Chapter 13 - Multi-Scale Modeling of Tissues Using CompuCell3D, in *Methods in Cell Biology*, Computational Methods in Cell Biology, Vol. 110, edited by A. R. Asthagiri and A. P. Arkin (Academic Press, 2012) pp. 325–366.
- [90] F. R. Cooper, R. E. Baker, M. O. Bernabeu, R. Bordas, L. Bowler, A. Bueno-Orovio, H. M. Byrne, V. Carapella, L. Cardone-Noott, J. Cooper, S. Dutta, B. D. Evans, A. G. Fletcher, J. A. Grogan, W. Guo, D. G. Harvey, M. Hendrix, D. Kay, J. Kursawe, P. K. Maini, B. McMillan, G. R. Mirams, J. M. Osborne, P. Pathmanathan, J. M. Pitt-Francis, M. Robinson, B. Rodriguez, R. J. Spiteri, and D. J. Gavaghan, Chaste: Cancer, Heart and Soft Tissue Environment, *J. Open Source Softw.* **5**, 1848 (2020).
- [91] M. Meier-Schellersheim and G. Mack, SIMMUNE, a tool for simulating and analyzing immune system behavior (1999), arXiv:cs/9903017.
- [92] J. T. Daub and R. M. H. Merks, Cell-Based Computational Modeling of Vascular Morphogenesis Using Tissue Simulation Toolkit, in *Vascular Morphogenesis: Methods and Protocols*, edited by D. Ribatti (Springer, New York, NY, 2015) pp. 67–127.
- [93] J. Starruß, W. de Back, L. Bruschi, and A. Deutsch, Morpheus: a user-friendly modeling environment for multiscale and multicellular systems biology, *Bioinformatics* **30**, 1331 (2014).
- [94] I. M. Wortel and J. Textor, Artistoo, a library to build, share, and explore simulations of cells and tissues in the web browser, *eLife* **10**, e61288 (2021), publisher: eLife Sciences Publications, Ltd.
- [95] N. J. Savill and R. M. H. Merks, The Cellular Potts Model in Biomedicine, in *Single-Cell-Based Models in Biology and Medicine*, Mathematics and Biosciences in Interaction, edited by A. R. A. Anderson, M. A. J. Chaplain, and K. A. Rejniak (Birkhäuser, Basel, 2007) pp. 137–150.
- [96] M. Durand and E. Guesnet, An efficient cellular potts model algorithm that forbids cell fragmentation, *Comput. Phys. Commun.* **208**, 54–63 (2016).
- [97] M. Scianna and L. Preziosi, A node-based version of the cellular potts model, *Comput. Biol. Med.* **76**, 94–112 (2016).
- [98] K. D. Nnetu, M. Knorr, J. Käs, and M. Zink, The impact of jamming on boundaries of collectively moving weak-interacting cells, *New J. Phys.* **14**, 115012 (2012).
- [99] E.-M. Schötz, M. Lanio, J. A. Talbot, and M. L. Manning, Glassy dynamics in three-dimensional embryonic tissues, *J. R. Soc. Interface* **10**, 20130726 (2013), publisher: Royal Society.
- [100] L. Bocanegra-Moreno, A. Singh, E. Hannezo, M. Zagorski, and A. Kicheva, Cell cycle dynamics control fluidity of the developing mouse neuroepithelium, *Nat. Phys.* , 1 (2023), publisher: Nature Publishing Group.
- [101] E. Hannezo and C.-P. Heisenberg, Rigidity transitions in development and disease, *Trends Cell Biol.* **32**, 433–444 (2022).
- [102] S. Garcia, E. Hannezo, J. Elgeti, J.-F. Joanny, P. Silberzan, and N. S. Gov, Physics of active jamming during collective cellular motion in a monolayer, *Proc. Natl. Acad. Sci. U.S.A.* **112**, 15314–15319 (2015).
- [103] E. Lawson-Keister and M. L. Manning, Jamming and arrest of cell motion in biological tissues, *Curr. Opin. Cell Biol.* **72**, 146–155 (2021).
- [104] T. E. Angelini, E. Hannezo, X. Trepas, M. Marquez, J. J. Fredberg, and D. A. Weitz, Glass-like dynamics of collective cell migration, *Proc. Natl. Acad. Sci. U.S.A.* **108**, 4714 (2011), publisher: Proceedings of the National Academy of Sciences.
- [105] D. Bi, J. H. Lopez, J. M. Schwarz, and M. L. Manning, Energy barriers and cell migration in densely packed tissues, *Soft Matter* **10**, 1885 (2014), publisher: The Royal Society of Chemistry.
- [106] E. C. Thomas and S. Hopyan, Shape-driven confluent rigidity transition in curved biological tissues, *Biophys. J.* **122**, 4264–4273 (2023).
- [107] S. Pandey, S. Kolya, S. Sadhukhan, and S. K. Nandi, The unusual glassy dynamics of confluent epithelial monolayer is nearly ideal for mode-coupling theory (2023), arXiv:2306.07250 [cond-mat, physics:physics].
- [108] P.-F. Lenne and V. Trivedi, Sculpting tissues by phase transitions, *Nat. Commun.* **13**, 664 (2022), publisher: Nature Publishing Group.
- [109] N. I. Petridou, B. Corominas-Murtra, C.-P. Heisenberg, and E. Hannezo, Rigidity percolation uncovers a structural basis for embryonic tissue phase transitions, *Cell* **184**, 1914 (2021).
- [110] M. Chiang and D. Marenduzzo, Glass transitions in the cellular potts model, *EPL* **116**, 28009 (2016).
- [111] S. Sadhukhan and S. K. Nandi, Theory and simulation for equilibrium glassy dynamics in cellular potts model

- of confluent biological tissue, *Phys. Rev. E* **103**, 062403 (2021).
- [112] A. J. Devanny, D. J. Lee, L. Kampman, and L. J. Kaufman, Signatures of jamming in the cellular potts model (2023).
- [113] M. Durand and J. Heu, Thermally driven order-disorder transition in two-dimensional soft cellular systems, *Phys. Rev. Lett.* **123**, 188001 (2019).
- [114] R. B. Potts, Some generalized order-disorder transformations, *Math. Proc. Camb. Philos. Soc.* **48**, 106–109 (1952).
- [115] 102 Single-Layered Squamous Epithelium—Mesentery, in *Color Atlas of Cytology, Histology, and Microscopic Anatomy*, edited by W. Kühnel (Georg Thieme Verlag KG, 2003) 4th ed., p. 102.
- [116] M. S. Steinberg, Differential adhesion in morphogenesis: a modern view, *Curr. Opin. Genetics Dev.* **17**, 281–286 (2007).
- [117] J. L. Antonakos and K. C. Mansfield, *Practical data structures using C/C++* (1999) pp. 165–190.
- [118] R. Allena, M. Scianna, and L. Preziosi, A Cellular Potts Model of single cell migration in presence of durotaxis, *Math. Biosci.* **275**, 57 (2016).
- [119] N. Guisoini, K. I. Mazzitello, and L. Diambra, Modeling Active Cell Movement With the Potts Model, *Front. Phys.* **6**, 61 (2018).
- [120] E. G. Rens and L. Edelstein-Keshet, From energy to cellular forces in the Cellular Potts Model: An algorithmic approach, *PLoS Comput. Biol.* **15**, e1007459 (2019).
- [121] R. Magno, V. A. Grieneisen, and A. F. Marée, The biophysical nature of cells: potential cell behaviours revealed by analytical and computational studies of cell surface mechanics, *BMC Biophys.* **8**, 8 (2015).
- [122] H. X. Zhu, S. M. Thorpe, and A. H. Windle, The geometrical properties of irregular two-dimensional voronoi tessellations, *Philos. Mag. A* **81**, 2765–2783 (2001).
- [123] S. Kumar and S. K. Kurtz, Properties of a two-dimensional poisson-voronoi tessellation: A monte-carlo study, *Mater. Charact.* **31**, 55–68 (1993).
- [124] C. H. Rycroft, VORO++: A three-dimensional Voronoi cell library in C++, *Chaos* **19**, 041111 (2009), https://pubs.aip.org/aip/cha/article-pdf/doi/10.1063/1.3215722/13277008/041111_1_online.pdf.
- [125] C. A. Schneider, W. S. Rasband, and K. W. Eliceiri, Nih image to imagej: 25 years of image analysis, *Nature Methods* **9**, 671–675 (2012).
- [126] P. Digregorio, D. Levis, A. Suma, L. F. Cugliandolo, G. Gonnella, and I. Pagonabarraga, Full phase diagram of active brownian disks: From melting to motility-induced phase separation, *Phys. Rev. Lett.* **121**, 098003 (2018).
- [127] J. R. Borba, C. Brito, P. Migowski, T. B. Vale, D. A. Stariolo, S. R. Teixeira, and A. F. Feil, Quantitative Characterization of Hexagonal Packings in Nanoporous Alumina Arrays: A Case Study, *J. Phys. Chem. C* **117**, 246 (2013), publisher: American Chemical Society.
- [128] M. Krajnc, Solid–fluid transition and cell sorting in epithelia with junctional tension fluctuations, *Soft Matter* **16**, 3209–3215 (2020).
- [129] J.-j. Li, Y.-l. He, and B.-q. Ai, Solid–liquid transition induced by rigidity disparity in a binary mixture of cell tissues, *Soft Matter* **19**, 3849–3858 (2023).
- [130] J. Žunić and K. Hirota, Measuring shape circularity, in *Progress in Pattern Recognition, Image Analysis and Applications* (Springer Berlin Heidelberg, 2008) p. 94–101.
- [131] J. Žunić, K. Hirota, and P. L. Rosin, A hu moment invariant as a shape circularity measure, *Pattern Recognit.* **43**, 47–57 (2010).
- [132] M.-K. Hu, Visual pattern recognition by moment invariants, *IEEE Trans. Inf. Theory* **8**, 179–187 (1962).
- [133] M. W. Nasrudin, N. S. Yaakob, N. A. Abdul Rahim, M. Z. Zahir Ahmad, N. Ramli, and M. S. Aziz Rashid, Moment invariants technique for image analysis and its applications: A review, *J. Phys. Conf. Ser.* **1962**, 012028 (2021).
- [134] L. Kopanja, Z. Kovacevic, M. Tadic, M. C. Žužek, M. Vrecl, and R. Frangež, Confocal micrographs: automated segmentation and quantitative shape analysis of neuronal cells treated with osteolysin a/pleurotolysin b pore-forming complex, *Histochem. Cell Biol.* **150**, 93–102 (2018).
- [135] M. Ammar, K. Baiche, S. Mahmoudi, and M. Benazzouz, Shape irregularity based area measurement: Application on cell nucleus recognition, in *2017 5th International Conference on Electrical Engineering - Boumerdes (ICEE-B)* (IEEE, 2017).
- [136] A. Pasupalak, L. Yan-Wei, R. Ni, and M. Pica Ciamarra, Hexatic phase in a model of active biological tissues, *Soft Matter* **16**, 3914–3920 (2020).
- [137] J.-j. Li and B.-q. Ai, Melting of two-dimensional biological tissues containing active ornstein–uhlenbeck cells, *New J. Phys.* **23**, 083044 (2021).
- [138] L. Atia, D. Bi, Y. Sharma, J. A. Mitchel, B. Gweon, S. A. Koehler, S. J. DeCamp, B. Lan, J. H. Kim, R. Hirsch, A. F. Pegoraro, K. H. Lee, J. R. Starr, D. A. Weitz, A. C. Martin, J.-A. Park, J. P. Butler, and J. J. Fredberg, Geometric constraints during epithelial jamming, *Nat. Phys.* **14**, 613–620 (2018).
- [139] D. J. Cislo, F. Yang, H. Qin, A. Pavlopoulos, M. J. Bowick, and S. J. Streichan, Active cell divisions generate four-fold orientationally ordered phase in living tissue, *Nat. Phys.* **19**, 1201–1210 (2023).
- [140] D. A. Sun and N. H. Patel, The amphipod crustacean parhyale hawaiiensis: An emerging comparative model of arthropod development, evolution, and regeneration, *Wiley Interdiscip. Rev. Dev. Biol.* **8**, e355 (2019).
- [141] A.-K. Classen, K. I. Anderson, E. Marois, and S. Eaton, Hexagonal packing of drosophila wing epithelial cells by the planar cell polarity pathway, *Dev. Cell* **9**, 805–817 (2005).
- [142] F. Pilot and T. Lecuit, Compartmentalized morphogenesis in epithelia: From cell to tissue shape, *Dev. Dyn* **232**, 685–694 (2005).
- [143] B. Aigouy, R. Farhadifar, D. B. Staple, A. Sagner, J.-C. Röper, F. Jülicher, and S. Eaton, Cell flow reorients the axis of planar polarity in the wing epithelium of drosophila, *Cell* **142**, 773–786 (2010).
- [144] T. Hayashi and R. W. Carthew, Surface mechanics mediate pattern formation in the developing retina, *Nature* **431**, 647–652 (2004).
- [145] H. Togashi, S. R. Davis, and M. Sato, From soap bubbles to multicellular organisms: Unraveling the role of cell adhesion and physical constraints in tile pattern formation and tissue morphogenesis, *Dev. Biol.* **506**, 1–6 (2024).
- [146] T. Lecuit and P.-F. Lenne, Cell surface mechanics and the control of cell shape, tissue patterns and morphogenesis, *Nat. Rev. Mol. Cell Biol* **8**, 633–644 (2007).

- [147] M. C. Gibson, A. B. Patel, R. Nagpal, and N. Perrimon, The emergence of geometric order in proliferating metazoan epithelia, *Nature* **442**, 1038–1041 (2006).
- [148] D. Ortolan, R. Sharma, A. Volkov, A. Maminishkis, N. A. Hotaling, L. A. Huryn, C. Cukras, S. Di Marco, S. Bisti, and K. Bharti, Single-cell-resolution map of human retinal pigment epithelium helps discover subpopulations with differential disease sensitivity, *Proc. Natl. Acad. Sci. U.S.A.* **119**, e2117553119 (2022).
- [149] D. Napoli, M. Biagioni, F. Billeri, B. Di Marco, N. Orsini, E. Novelli, and E. Strettoi, Retinal pigment epithelium remodeling in mouse models of retinitis pigmentosa, *Int. J. Mol. Sci.* **22**, 5381 (2021).
- [150] S. T. Islam, C. Cheng, J. Parreno, and V. M. Fowler, Nonmuscle myosin iia regulates the precise alignment of hexagonal eye lens epithelial cells during fiber cell formation and differentiation, *Investig. Ophthalmol. Vis. Sci.* **64**, 20 (2023).
- [151] A. Jain, V. Ulman, A. Mukherjee, M. Prakash, M. B. Cuenca, L. G. Pimpale, S. Münster, R. Haase, K. A. Panfilio, F. Jug, S. W. Grill, P. Tomancak, and A. Pavlopoulos, Regionalized tissue fluidization is required for epithelial gap closure during insect gastrulation, *Nat. Commun* **11**, 5604 (2020).
- [152] S. B. Lemke and C. M. Nelson, Dynamic changes in epithelial cell packing during tissue morphogenesis, *Curr. Biol* **31**, R1098–R1110 (2021).
- [153] J. A. Zallen and R. Zallen, Cell-pattern disordering during convergent extension in *Drosophila*, *J. Phys. Condens. Matter* **16**, S5073–S5080 (2004).
- [154] A. Hočevár and P. Zihler, Degenerate polygonal tilings in simple animal tissues, *Phys. Rev. E* **80**, 011904 (2009).
- [155] R. I. Johnson, Hexagonal patterning of the *Drosophila* eye, *Dev. Biol.* **478**, 173–182 (2021).
- [156] O. Campàs, I. Noordstra, and A. S. Yap, Adherens junctions as molecular regulators of emergent tissue mechanics, *Nat. Rev. Mol. Cell Biol.* **25**, 252 (2024), publisher: Nature Publishing Group.
- [157] M. Luciano, M. Versaevel, E. Vercruyse, A. Procès, Y. Kalukula, A. Remson, A. Deridou, and S. Gabriele, Appreciating the role of cell shape changes in the mechanobiology of epithelial tissues, *Biophys. Rev.* **3**, 011305 (2022).
- [158] P. Gottheil, J. Lippoldt, S. Grosser, F. Renner, M. Saibah, D. Tschodu, A.-K. Poßögel, A.-S. Wegscheider, B. Ulm, K. Friedrichs, C. Lindner, C. Engel, M. Löffler, B. Wolf, M. Höckel, B. Aktas, H. Kubitschke, A. Niendorf, and J. A. Käs, State of Cell Unjamming Correlates with Distant Metastasis in Cancer Patients, *Phys. Rev. X* **13**, 031003 (2023), publisher: American Physical Society.
- [159] R. Alert and X. Trepat, Living cells on the move, *Phys. Today* **74**, 30 (2021).
- [160] S. Sadhukhan and S. K. Nandi, On the origin of universal cell shape variability in confluent epithelial monolayers, *eLife* **11**, e76406 (2022).
- [161] D. S. Roshal, K. Azzag, K. K. Fedorenko, S. B. Rochal, and S. Baghdiguian, Topological properties and shape of proliferative and nonproliferative cell monolayers, *Phys. Rev. E* **108**, 024404 (2023).
- [162] D. Sánchez-Gutiérrez, M. Tozluoglu, J. D. Barry, A. Pascual, Y. Mao, and L. M. Escudero, Fundamental physical cellular constraints drive self-organization of tissues, *EMBO J.* **35**, 77–88 (2015).
- [163] G. Zhang, R. Mueller, A. Doostmohammadi, and J. M. Yeomans, Active inter-cellular forces in collective cell motility, *J. R. Soc. Interface* **17**, 20200312 (2020).
- [164] D. L. Barton, S. Henkes, C. J. Weijer, and R. Sknepnek, Active vertex model for cell-resolution description of epithelial tissue mechanics, *PLOS Comput. Biol.* **13**, e1005569 (2017).
- [165] L. Yan and D. Bi, Multicellular rosettes drive fluid-solid transition in epithelial tissues, *Phys. Rev. X* **9**, 011029 (2019).
- [166] J. Huang, J. O. Cochran, S. M. Fielding, M. C. Marchetti, and D. Bi, Shear-driven solidification and nonlinear elasticity in epithelial tissues, *Phys. Rev. Lett.* **128**, 178001 (2022).
- [167] X. Li, A. Das, and D. Bi, Biological tissue-inspired tunable photonic fluid, *Proc. Natl. Acad. Sci. U.S.A.* **115**, 6650–6655 (2018).
- [168] O. Hallatschek, P. Hersen, S. Ramanathan, and D. R. Nelson, Genetic drift at expanding frontiers promotes gene segregation, *Proc. Natl. Acad. Sci. U.S.A.* **104**, 19926–19930 (2007).

Supplementary Information

A. Coexistence

The snapshot in Fig. 10 shows that regions of more disordered configurations, for which yellow cells are abundant, coexist with ordered parts of the simulation volume, as indicated by the larger purple regions in the bottom-right quadrant. The simulation was performed for a value of $\alpha = 2$, which lies in the transition region for an irregular lattice.

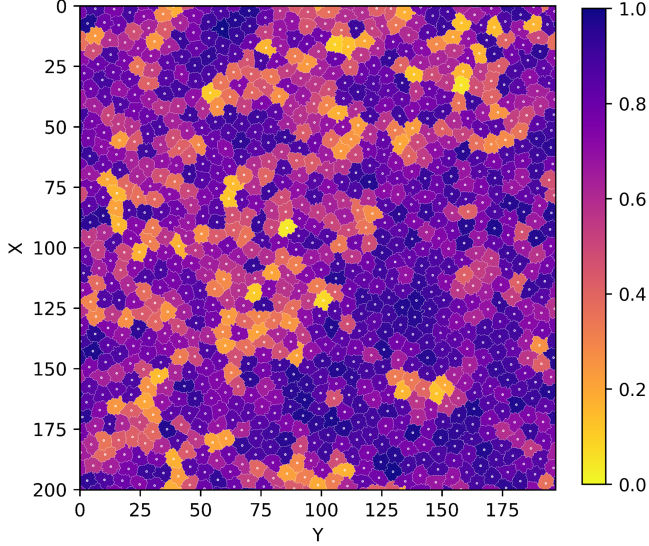


Figure 10. Simulation snapshot revealing the coexistence of the ordered and disordered phase. The surface tension parameter $\alpha = 2.0$ was chosen close to the transition point obtained for the irregular lattice. The white dots indicate the center of mass of the cells, while the color indicates the hexatic order.

B. Lattice artifacts

Figure 11 shows the probability density function (PDF) belonging to the hexatic order parameter $|\psi_6|$ as measured for a high value of $\alpha = 4$. The distribution shows a clear main peak lattice artifact for the underlying square lattice, with a potential secondary artifact distribution to the right of the vertical black line. Conversely, the distribution on the irregular lattice is smooth and shows no clear lattice artifacts.

C. Pseudo-polygons on regular lattices

Figure 12 shows the fractions of pseudo-polygons on square and hexagonal lattices. From Fig. 12a, it becomes clear that the argument we made about the crossover between f_6 and f_5 being an indicator of the phase transition on the irregular lattice, holds also for the square lattice. Figure 12b shows the fractions on the hexagonal lattice. It can be seen that although the ratio f_6/f_5 can be still a determinant of transition, there is a subtle mismatch in this type of lattice. This is commensurate with the notion that the hexagonal lattice favors the diffusion of hexag-

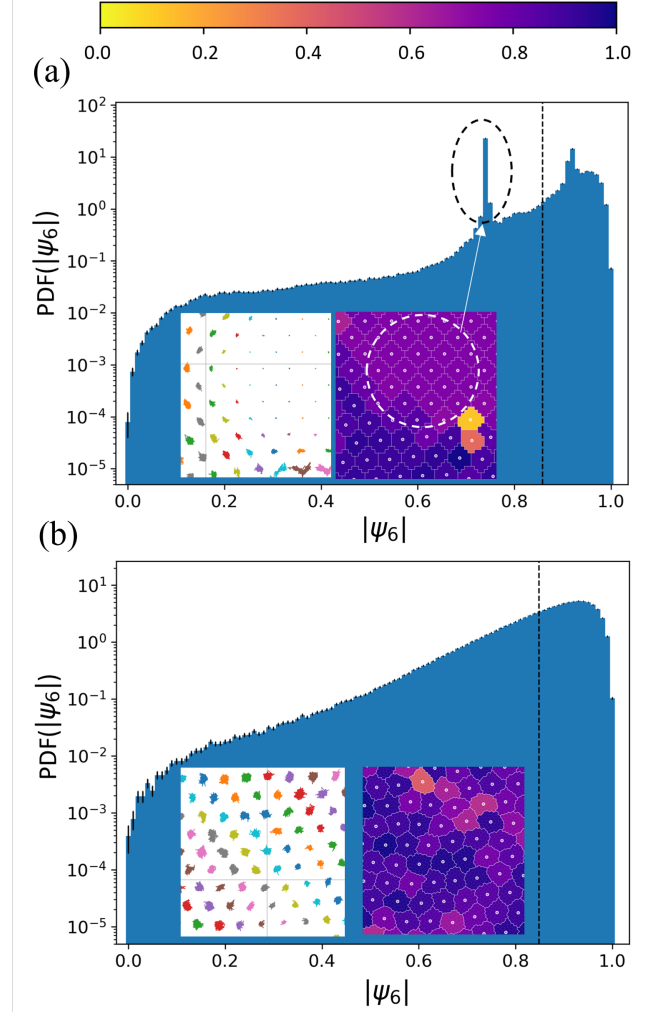


Figure 11. The lattice artifacts observed on the square lattice disappear on the disordered lattice. (a) The distribution (probability density function; PDF) of the hexatic order on the square lattice for $\alpha = 4$. The unphysical peak is indicated by the dashed ellipse. (b) The same distribution for the same value of α on the disordered lattice. The insets in both panels show the configurations of the cells and the trajectories of their centers of mass. On the right-hand side of the inset, the model cells are colored by the hexatic order parameter $|\psi_6|$, for which the color bar is shown at the top of the figure. The coloring on the left-hand side is to distinguish individual cells and has no physical significance. In both graphs, the error bars indicate the standard error of the mean and the vertical dashed line represents the average value of the distribution.

onal cells, thereby creating artificially high cell mobility for the crystal configuration.

D. q_V at the transition

The fractions shown in Fig. 7a in the main text derive from integrals of the q_V distributions. Since there are few other generalized polygons in the system, we can also relate the crossover to the median of the PDF for q_V , *i.e.*, whenever this median equals $q(n^* = 5.5)$. In other words,

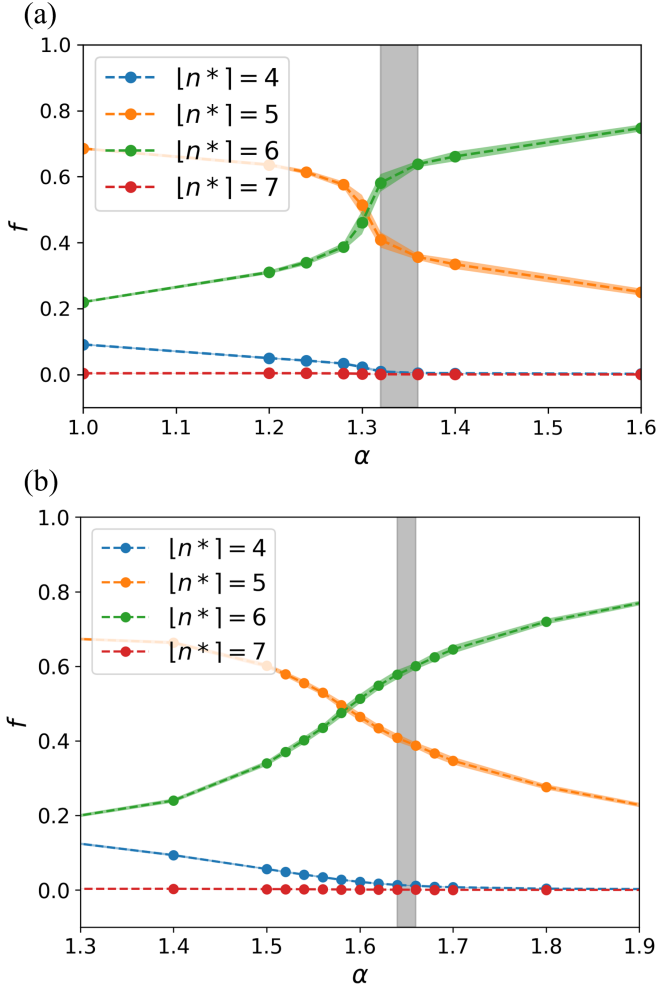


Figure 12. The fractions of pseudo-polygons f_{n^*} as a function of the surface tension α obtained for square (a) and hexagonal (b) lattices. The number of edges for the pseudo-polygons is indicated in the legend and the colored area around the respective curves indicates the standard error of the mean. The vertical gray bar shows the range for which the system transitions from a fluid to a hexagonal solid; the MSD exponent β exponent drops below 0.95. Note the mismatch for the hexagonal lattice.

we can consider $med(q_V)$ as a determinant of transition. One may also wonder how the mean of q_V behaves. Both of these quantities can be considered as indicators of the phase transition, whenever the fraction of other n^* -gons is low. Figure 13 provides these relations, revealing that the median appears to be slightly more predictive within the error.

E. n^* on regular lattices

Figure 14 shows the distribution of n^* parameter and the behavior of its extrema on the square and the hexagonal lattices. Like the irregular lattice, we see that the number of the extrema of this distribution determines the state. As we discussed for the irregular lattice, the

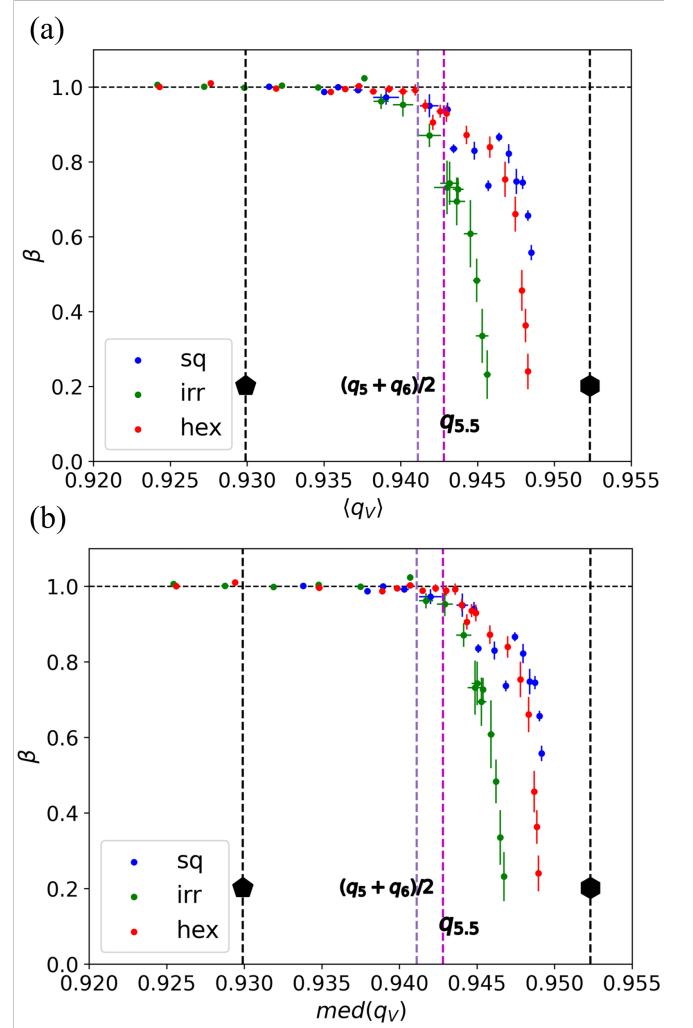


Figure 13. The long-time exponent of the mean-squared displacement β as a function of the average (a) and median (b) of the Voronoi-derived isoperimetric quotient q_V . The three underlying lattices are as indicated using the colors in the legends and the error bars indicate the standard error of the mean. The values of q_V for a pentagon and hexagon are indicated using vertical dashed lines and symbols. The derived values for a generalized ($n^* = 5.5$)-gon and the arithmetic mean of the hexagon and pentagon values are indicated using vertical dashed magenta and purple lines, respectively. The horizontal dashed black line indicates the value $\beta = 1$ for diffusive dynamics.

local minimum and the minor local maximum merge together and disappear at the transition, while the position of the global maximum experiences an abrupt change in its slope, and hardly changes in value beyond the transition. The global maximum at the transition is around $n^* \approx 5.7$, as was the case for the irregular lattice. However, as we see on the hexagonal lattice, the symmetries of the underlying lattice can change the nature of the transition to some extent.

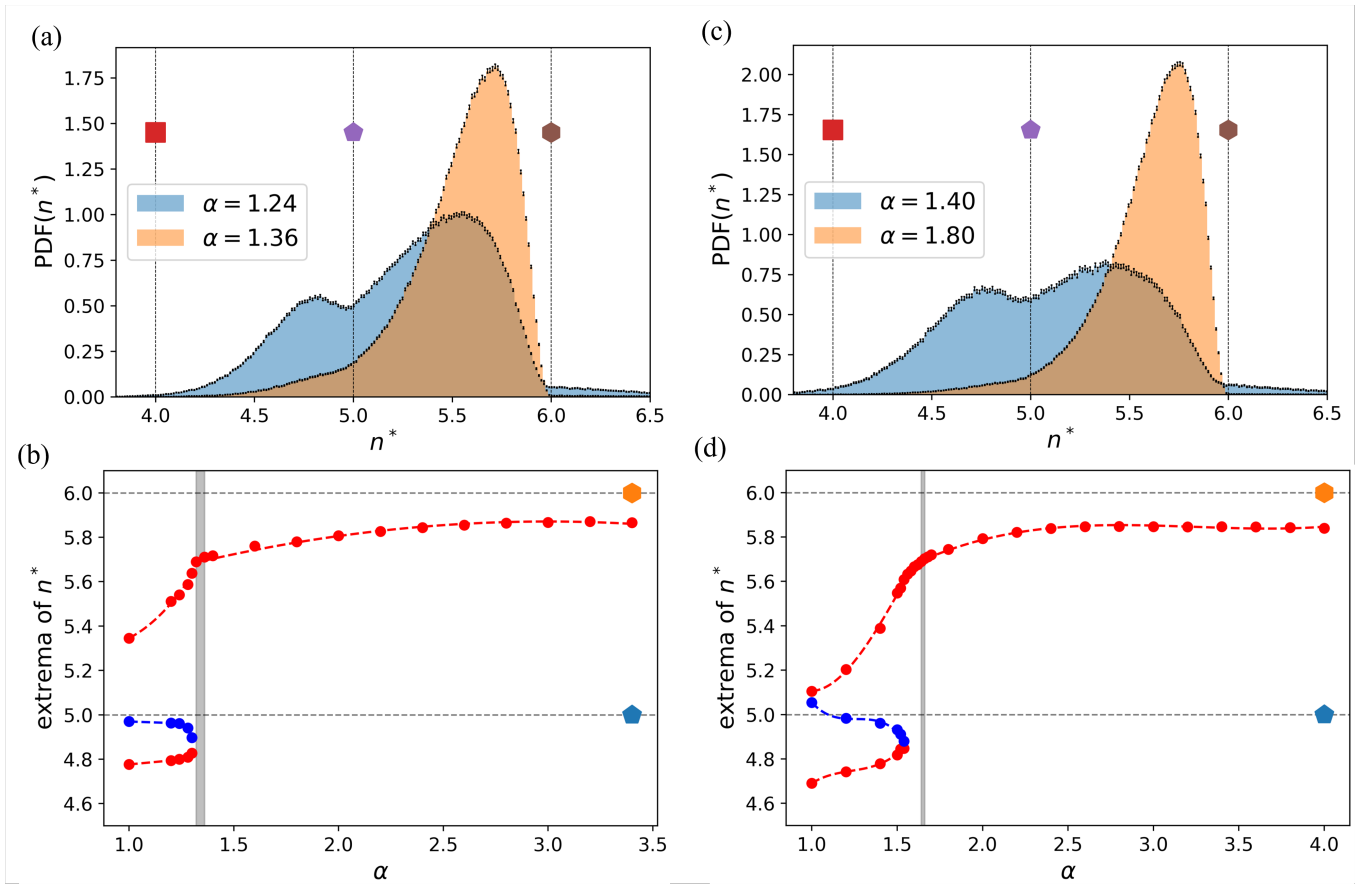


Figure 14. The distribution of n^* parameter indicates the phase transition on regular lattices, but less so on hexagonal lattices. (a) Distribution of n^* for two values of α are shown as well as the local minimum on the square lattice. For $\alpha = 1.24$ (blue) the tissue is fluid-like, while for $\alpha = 1.36$ (orange) it is solid-like. (b) The positions of the maxima (red) and the local minimum (blue) of n^* distribution on the square lattice are plotted as a function of α . The dashed lines are there to guide the eye, and the gray box indicates the transition point. (c,d) The analog of (a,b) for a hexagonal lattice, with a typical fluid-like ($\alpha = 1.4$, blue) and solid-like state ($\alpha = 1.8$, orange).

F. Circularity on regular lattices

Figure 15 shows the behavior of the mode of the Voronoi circularity on square and hexagonal lattices. Unlike the distributions of q_V and n^* , the distribution of C_V always has only a single peak. Nonetheless, the mode of this distribution is also a complementary determinant of

the transition. As for the irregular lattice we discussed in the main text, on the square lattice, the mode of C_V distribution equals the circularity of the pentagon. For the hexagonal lattice, like n^* , there is the expected mismatch.

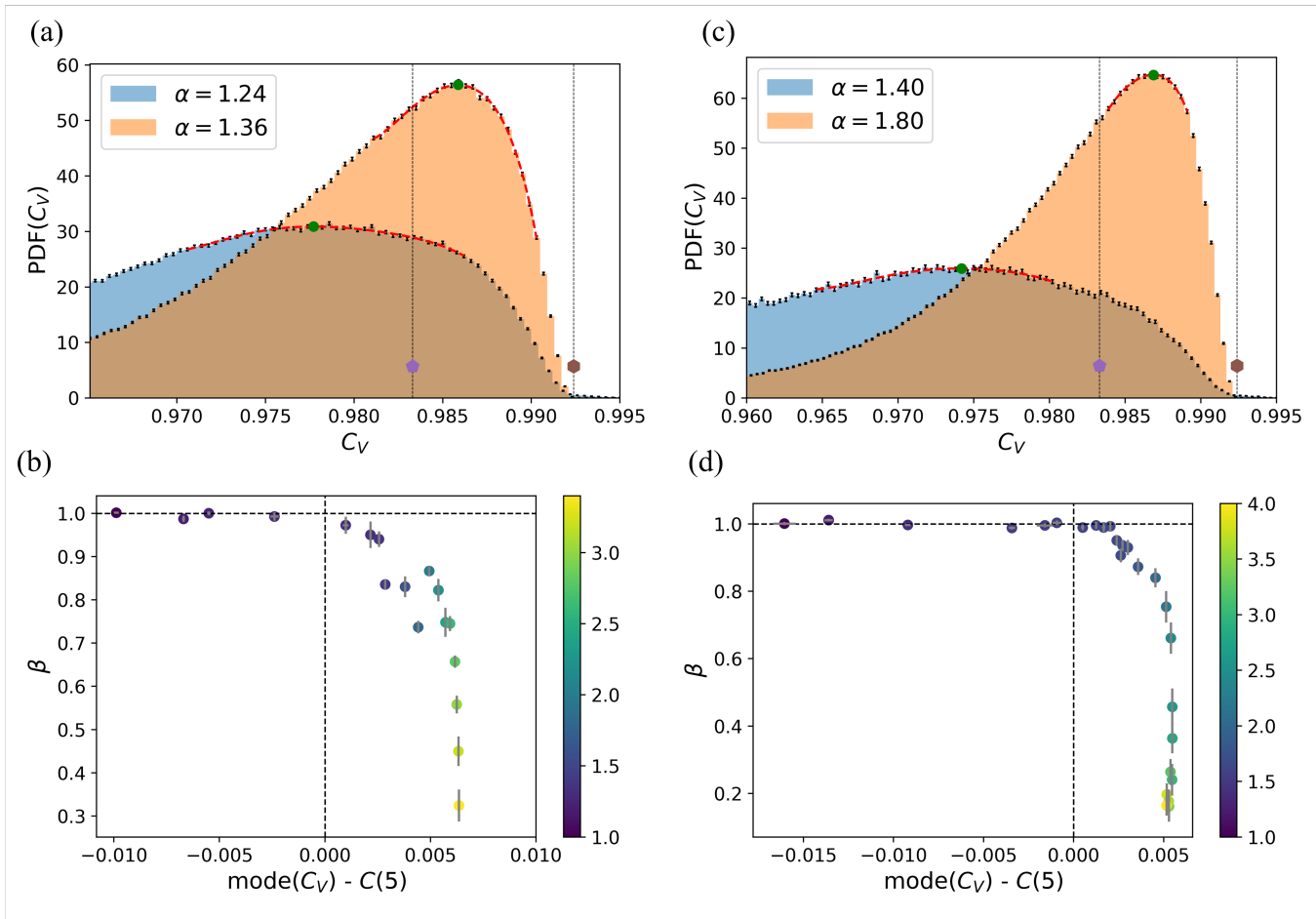


Figure 15. The mode of the Voronoi-based circularity indicates phase transition on regular lattices, but to a lesser degree for hexagonal lattices. (a) The PDF of the Voronoi-based circularity, C_V , for two values of α , one of which in fluid-like ($\alpha = 1.24$, blue) and the other in solid-like ($\alpha = 1.36$, orange) regime, on the square lattice. The positions of the peaks (green dots) are determined by polynomial fittings (red dashed lines). The vertical dashed lines show the values of circularity for the pentagon and hexagon. (b) The long-term MSD exponent, β , plotted as a function of the departure between the mode of C_V from the circularity of a pentagon, $C(5)$, on a square lattice. The data points are colored by the values of α as shown by the color bar on the right. The data of the highest 3 values of α are not plotted because of the considerable lattice artifacts. (c,d) The analog of (a,b) for a hexagonal lattice, with a typical fluid-like ($\alpha = 1.4$, blue) and solid-like state ($\alpha = 1.8$, orange).